Journal of Petrology Advance Access published June 3, 2005

Phase Relations and Chemical Composition of Phengite and Paragonite in Pelitic Schists During Decompression: a Case Study from the Monte Rosa Nappe and Camughera–Moncucco Unit, Western Alps

L. M. KELLER*, R. ABART, S. M. SCHMID AND C. DE CAPITANI

DEPARTMENT OF EARTH SCIENCES, BASEL UNIVERSITY, BERNOULLISTRASSE 32, CH-4056 BASEL

RECEIVED NOVEMBER 25, 2003; ACCEPTED APRIL 12, 2005

The metamorphic evolution of metapelites from the eastern part of the Monte Rosa nappe and the Camughera–Moncucco unit, both situated in the upper Penninic units SW of the Simplon line, were investigated using microstructural relationships and equilibrium phase diagrams. The units under consideration experienced pre-Alpine amphibolite-facies conditions and underwent a complex metamorphic evolution during the Alpine orogeny. Peak pressures during an early Alpine high-pressure stage of 12·5–16 kbar were similar in the Monte Rosa nappe and Camughera–Moncucco unit. A pronounced thermal gradient is indicated during decompression leading to an amphibolite-facies overprint, as the decompression paths went through the chlorite, biotite and plagioclase stability fields in most of the Monte Rosa nappe, through the staurolite field in the easternmost Monte Rosa nappe and in the Camughera–Moncucco unit, and through the sillimanite field in the easternmost Camughera–Moncucco unit. In high-Al metapelites the initial formation of staurolite is related to continuous paragonite breakdown and associated formation of biotite. In the course of this reaction phengite becomes successively sodium enriched. In low-Al metapelites, in contrast, the initial staurolite formation occurs via the continuous breakdown of sodium-rich phengite. In both low- and high-Al metapelites the largest volume of staurolite is formed during the continuous breakdown of sodium-rich phengite below P–T *conditions of about 9·5 kbar at 600–650° C. During this reaction phengite becomes successively potassium enriched as sodium from phengite is used to form the albite component in plagioclase. For 'normal' pelitic chemistries, phengite becomes Na enriched during decompression through the breakdown of paragonite along a near-isothermal decompression path. The Na content in phengite reaches its maximum when paragonite is entirely consumed. During further decompression the paragonite component in phengite decreases again because Na is preferentially incorporated into the albite component of plagioclase.*

KEY WORDS: *metapelites; white mica; high pressure; equilibrium diagrams; Western Alps*

INTRODUCTION

Regional Barrovian-type metamorphism of pelitic rocks is characterized by a sequence of mineral zones, which mimic progressive metamorphism from chlorite through biotite, staurolite, kyanite and sillimanite zones (Barrow, 1912). These mineral zones have been found in many areas and are commonly considered typical for prograde medium-pressure metamorphism. It is important to note, however, that such mineral zones need not necessarily reflect a single P–T path. They may rather reflect mineral assemblages formed during particular stages during the P–T evolution, which were attained along different P–T paths. The reaction history (i.e. the sequence of equilibrium assemblages within a single metamorphic unit) depends on the trajectory of the associated specific P–T path the unit experienced. In particular, reaction histories will be different depending on whether the metamorphic assemblage was formed on a prograde P–T path

*Corresponding author. Fax: 0041/(0) 61 267 36 13. E-mail: Lukas.Keller@unibas.ch

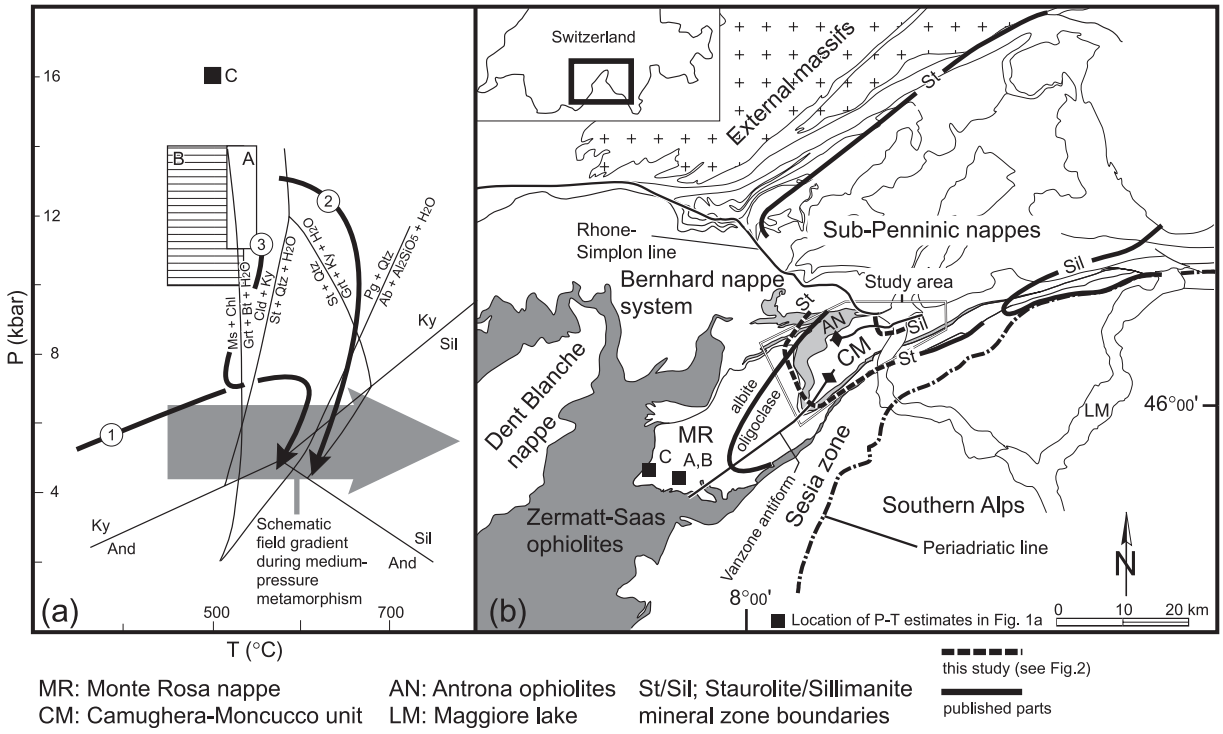

Fig. 1. *P–T* conditions of metamorphism and tectonic map of the study area. (a) *P–T* grid and mineral reactions modified after Bucher & Frey (1994). A, B and C indicate *P–T* conditions during high-pressure metamorphism for the western Monte Rosa nappe: A, Borghi *et al.* (1996); B, Dal Piaz & Lombardo (1986); C, Chopin & Monié (1984). 1, 2 and 3 are three *P–T* paths (hypothetically drawn) representing: 1, a temperature-dominated path; 2, near-isothermal decompression; 3, decompression followed by a heating pulse. The selected equilibria and *P–T* paths show that the formation of particular mineral assemblages and/or mineral zone boundaries typical for Barrovian metamorphism, and formed at moderate pressures, may have formed during the late stage of very different *P–T* paths. The grey arrow schematically represents the metamorphic field gradient during medium-pressure metamorphism. (b) Modified tectonic map of the western part of the Penninic Alps, after Spicher (1976) and Keller & Schmid (2001), showing the outline of the study area, the mineral zone boundaries characteristic for the Barrovian metamorphism in the study area and the location of the *P–T* estimates given in (a). Sillimanite and staurolite mineral zone boundaries are after Niggli (1970) and this study (see Fig. 2). The albite–oligoclase isograd is after Bearth (1958).

during temperature increase (*P–T* path 1 in Fig. 1a), or during nearly isothermal decompression (*P–T* path 2 in Fig. 1a).

In the case of the classical European Alpine collisional orogen (Schmid *et al.*, 2004), prograde medium-pressure metamorphism has been reported, for example, from the Lukmanier area in the northern central Alps (Fox, 1975) (*P–T* path 1 in Fig. 1a). In this case, the mineral zones characterize progressive metamorphism from the Cld + Chl + Ky through St + Cld + Chl + Ky, Bt + St + Cld + Chl + Ky and Bt + St + Grt + Chl + Ky zones (Fox, 1975). A different metamorphic evolution is reported from the southern parts of the Adula nappe in the central Alps, where Barrovian metamorphism occurred during decompression from a precursory high-pressure stage (Heinrich, 1986; Meyre *et al.*, 1997, 1999; Nagel *et al.*, 2002). Barrovian metamorphism during decompression has also been reported from the southern Koralpe (eastern Alps) (Gregurek *et al.*, 1997).

In the case of the central Alps (Adula nappe), Nagel *et al.* (2002) proposed the formation of mineral assemblages containing staurolite, kyanite and sillimanite during approximately isothermal decompression (*P–T* path 2 in Fig. 1a). However, other workers have suggested that a heating pulse did occur during a later stage of Tertiary metamorphism in the southern parts of the Lepontine area (*P–T* path 3 in Fig. 1a) (e.g. Becker, 1993; Engi *et al.*, 1995; Todd & Engi, 1997). The modelling by Engi *et al.* (2001*b*) suggests *P–T* paths from the Central Alps that involve a heating stage after decompression. Heating is induced by accretion of continental crustal fragments with higher radioactive heat production. Hence, it is still a matter of debate whether Barrovian metamorphism in the more southern part of the Central Alps and adjacent gneissic units of the upper Penninic Alps is associated with, or without, substantial reheating that post-dates decompression. To discuss the nature of Barrovian metamorphism in the light of the above-mentioned controversy, this study focuses on the gneissic units of the upper Penninic Alps, situated SW of the Simplon line (Fig. 1), where the metamorphic characteristics are similar to those of the Adula nappe. These characteristics involve

an early regional Alpine high-pressure overprint in the Zermatt–Saas ophiolites, Monte Rosa nappe and Antrona ophiolites (Fig. 1b) (Frey *et al.*, 1999). During later stages all these units, including the Camughera–Moncucco (CM) unit, underwent medium-pressure metamorphism characterized by a metamorphic field gradient indicating an increase in temperature from the west to the east and towards deeper structural levels (Fig. 1b) (see below). In the case of the gneissic unit under consideration, the CM unit, it is even unclear whether it experienced an earlier high-pressure event or not. Hence, this study aims to reveal the various P–T paths (Fig. 1a), along which the assemblages typical for Barrovian metamorphism in the CM unit were formed. Generally speaking, this study contributes towards the characterization of metamorphic areas that experienced Barrovian metamorphism.

To unravel the metamorphic history of the gneissic units SW of the Simplon line a sequence of stable mineral assemblages is established on the basis of microstructural relationships. In addition, the variation of the paragonite and celadonite content of phengite is used to unravel the metamorphic history. Phase relations are investigated for different bulk-rock compositions to test the sensitivity of mineral assemblages to bulk-rock compositions.

GEOLOGICAL SETTING

Tectonic context

The Monte Rosa nappe, Antrona ophiolites and CM unit belong to the upper Penninic nappe pile west of the Lepontine dome and SE of the Simplon line (Fig. 1b). As a result of south-vergent backfolding associated with an axial plunge towards the SW, the former nappe pile can be seen as a distorted profile in map view (e.g. Klein, 1978; Milnes *et al.*, 1981; Escher *et al.*, 1997). The CM unit is the structurally deepest unit of this part of the western Alps, being situated in the core of the Vanzone antiform (e.g. Bearth, 1957) (Fig. 1b). The CM unit is mainly composed of pre-Mesozoic paragneisses and orthogneisses (e.g. Bearth, 1956; Laduron, 1976; Merlyn, 1977). The Antrona ophiolites separate the CM unit from the Monte Rosa nappe, which itself is overlain by the Zermatt–Saas ophiolites (Fig. 1b). The pre-Alpine protoliths of the Monte Rosa nappe consist of metapelitic paragneisses, intruded by post-Variscan granites at around 310 and 270 Ma (Hunziker, 1970; Frey *et al.*, 1976).

High-pressure metamorphism

According to the metamorphic maps of the Alps (Frey *et al.*, 1999; Oberhänsli *et al.*, 2004) the Zermatt–Saas ophiolites, Monte Rosa nappe and Antrona ophiolites all have undergone a regional high-pressure metamorphism. Recent isotopic studies indicate an Early to Middle Eocene age for the high-pressure stage in the Zermatt–Saas ophiolites (Bowtell *et al.*, 1994; Rubatto *et al.*, 1997).

An Eocene to early Oligocene age is considered for the high-pressure metamorphism in the internal crystalline massifs (e.g. Duchene *et al.*, 1997; Dal Piaz, 1999). P–T estimates for the high-pressure stage in the Monte Rosa nappe are in the range of 8–10 kbar and <14 kbar, at temperatures of 440–530°C (Dal Piaz & Lombardo, 1986). Also for the high-pressure stage, but based on the Grt–Phe geothermometer and geobarometry based on the Si content in phengite, Borghi *et al.* (1996) derived P–T estimates in the range of 518–546°C at 11–14 kbar. Somewhat higher pressures (16 kbar at 500°C) were obtained by Chopin & Monié (1984) for an atypical mineral assemblage found in a pelitic sample from the Monte Rosa nappe. Regarding the high-pressure stage of the Antrona ophiolites Colombi & Pfeifer (1986) inferred P–T conditions of >14 kbar at 500–700°C.

Medium-pressure metamorphism

During a late stage of Alpine metamorphism the eastern part of the Monte Rosa nappe, the Antrona ophiolites and the CM unit experienced amphibolite-facies conditions, whereas the western part of the Monte Rosa nappe only reached the greenschist facies (Frey *et al.*, 1999). This metamorphic zonation was first recognized by Bearth (1958), who mapped the albite–oligoclase boundary in the study area (Fig. 1b), indicating a metamorphic field gradient with temperatures increasing from west to east. The temperatures estimated for the Antrona ophiolites range between 600 and 700°C (Colombi, 1989, fig. 6–2E). For the CM unit no quantitative P–T estimates are available so far and it is not known whether this unit underwent an early high-pressure metamorphic stage at all. Within the CM unit several occurrences of staurolite and kyanite are known (Merlyn, 1977, fig. 14). For the more eastern parts of the Monte Rosa nappe Engi *et al.* (2001*a*) estimated P–T conditions ranging between 9 and 12 kbar at 595–755°C interpreted to represent partial re-equilibration upon decompression.

METHODS OF INVESTIGATION

Petrography

The mineral compositions were determined with a JEOL JXA-8600 electron microprobe at 15 kV acceleration voltage and 10 nA sample current and correcting with a PROZA routine. The mole fractions of the end-members muscovite, paragonite, Mg-celadonite and Fe-celadonite in white mica were calculated by applying the method of least squares.

Equilibrium phase diagrams

Equilibrium phase diagrams were calculated with the program DOMINO (De Capitani & Brown, 1987; De Capitani, 1994), using the database of Berman (1988, update 1992). The following thermodynamic data and solution models were used: (1) staurolite and chloritoid, the thermodynamic data of Nagel *et al.* (2002); (2) garnet, the solution model of Berman (1990); (3) biotite, binary (Phl, Ann) ideal mixing on site (3); (4) chlorite, the solution model of Hunziker (2003); (5) feldspar, the solution model of Fuhrman & Lindsley (1988); (6) omphacite, the solution model of Meyre *et al.* (1997); (7) staurolite, the solution model of Nagel *et al.* (2002); (8) white mica, the solution model of Keller *et al.* (2005*a*); (9) chloritoid, binary ideal mixing on site (1).

Whole-rock chemistry

Whole-rock compositions were determined on fused pellets by X-ray fluorescence (XRF) using a Bruker AXS SRS-3400 at the Geochemical Laboratory in Basel. From each sample one slice was cut. From these slices one thin section was prepared and from the remaining volume the layers containing the indicative mineral assemblages were extracted and analysed. Whole-rock chemistries of the studied samples are presented in Table 1.

Table 1: Bulk-rock compositions of the investigated samples and published average rock compositions of high-grade metapelites

	LK13	LK45	LK48	LK76	1	4	P1	P2
SiO_2	57·17	44·37	59·47	60·63	49·04	59·04	60·26	56·25
Al_2O_3	19·25	32·41	22·38	20·55	29·84	21·96	20·64	20·18
FeO							5·49	
Fe_2O_3	9·10	11·11	6·42	8·45	8·60	7·78	1·41	9·31
MnO	0·10	0·12	0·09	0·07	0·15	0·11		0·18
MgO	3·93	2·04	1·88	2·60	2·05	2·01	1·93	3·23
CaO	1·34	0·35	0·21	0·35	0·33	0·50	0·52	1·54
Na_2O	2·33	1·00	1·13	0·66	1·41	1·29	1·38	1·80
K_2O	3·31	4·70	4·71	3·61	5·00	3·94	3·72	4·02
TiO_2	0·90	1·08	0·89	0·94	1·07	0·84	1·05	1·05
P_2O_5	0·11	0·07	0·15	0·08	0·10	0·14		
Sum	97·54	97·25	97·33	97·94	97·59	97·60	96·4	97·56

P1, medium- and high-grade pelites of Shaw (1956); P2, amphibolite-facies pelites of Ague (1991).

Succession of metamorphic stages

To derive the *P–T* history of the metapelitic rocks from the study area we selected six samples containing well-preserved microstructural relationships. Two of the six samples (samples 1 and 4) were described by Keller *et al.* (2004), and are representative of the high-pressure overprint of pre-Alpine metamorphic pelites during an early stage of Alpine metamorphism. This early stage marks the starting point of the subsequent decompression history. Hence the physical conditions and mineral chemistries related to this early high-pressure stage will be discussed in some detail. As will be demonstrated, the remaining samples from the CM unit record subsequent decompression stages during the Alpine metamorphic cycle.

Figure 2 illustrates the regional distribution of the minerals staurolite and sillimanite, and also shows the proposed staurolite and sillimanite mineral zone boundaries for the gneissic units SW of the Simplon line (see also Fig. 1b). These mineral zone boundaries indicate a metamorphic field gradient with temperatures increasing towards the east and towards deeper structural levels. This is in line with the albite–oligoclase isograd of Bearth (1958) (Fig. 1b) and the pattern of regional isotherms established by Colombi (1989) and Todd & Engi (1997). The proposed staurolite mineral zone boundary is also constrained by the studies of Laduron (1976), Merlyn (1977) and Engi *et al.* (2001*a*), which reported no staurolite-bearing metapelites SW of this proposed mineral zone boundary. The southeastern part of the mineral zone boundary was mapped by Reinhardt (1966) (Fig. 2).

Bulk-rock chemistry

Because the sequence of mineral assemblages may be sensitive to bulk-rock composition, the bulk-rock chemistries of the investigated samples are presented first (Table 1), before discussing the microstructures. In addition, average chemical compositions of medium- and high-grade pelitic rocks described by Shaw (1956, Table 5) and by Ague (1991, Table 2) are also given. These bulk-rock compositions are compared in a kind of AFM projection (Thompson, 1957) in Fig. 3. For calculation of the AFM coordinates the amounts of Al_2O_3 bound by CaO in anorthite and those of Na_2O bound in paragonite were subtracted from the total Al_2O_3. The resulting projection is referred to as an A′FM projection (Laduron, 1976). Sample LK13 and the average composition of Ague (1991) both plot at lower A′ values than the other samples, despite the fact that these two compositions are not so low in total Al_2O_3 (Table 1). This is explained by the fact that sample LK13 and the average composition of Ague (1991) are enriched in CaO and Na_2O, both binding Al_2O_3 in specific minerals (plagioclase and paragonite in our case) and thereby reducing the A′ value in the A′FM plane. Thus, the CaO and Na_2O bulk-rock contents may influence the development of mineral assemblages, as indicated by the scattered distribution of bulk-rock chemistries in

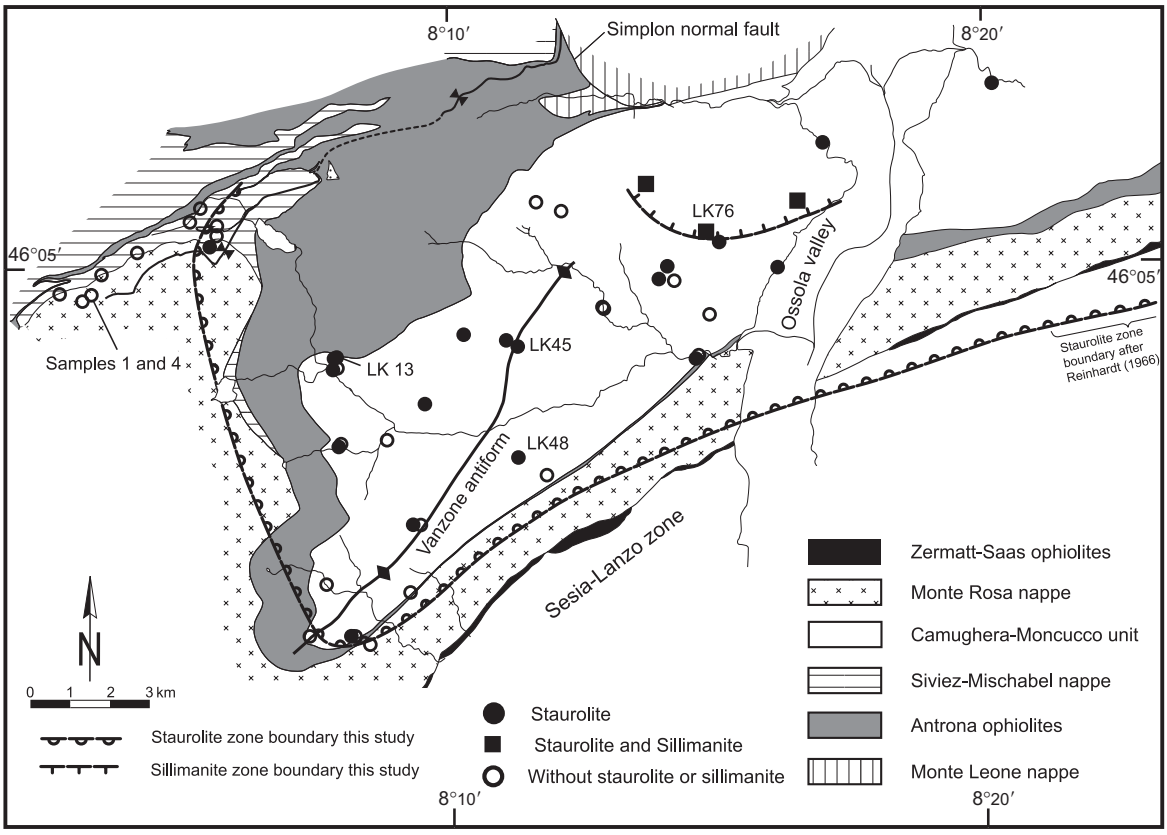

Fig. 2. Tectonic map of the study area outlined in Fig. 1, showing the distribution of staurolite and sillimanite and the location of the mineral zone boundaries. The southeastern part of the staurolite mineral zone boundary was mapped by Reinhardt (1966).

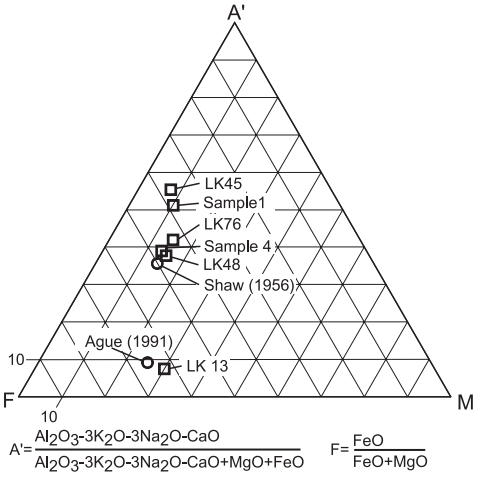

Fig. 3. A′FM triangular plot derived from the classical AFM projection. This illustrates the bulk-rock compositions of the samples investigated and the published average pelitic compositions of Shaw (1956) and Ague (1991).

the A′FM plane. Because of its low A′ value sample LK13 is regarded as representing the metamorphic evolution of low-Al pelites. The compositions of samples 4, LK48 and LK76 plot within a narrow field close to the average pelitic composition of Shaw (1956). Hence it is most likely that these three samples preserve assemblages corresponding to successive stages of the metamorphic history of medium-Al pelites in the study area. Samples 1 and LK45 plot at higher A′ values (high-Al pelites) compared with all other samples.

Early high-pressure overprint of the pre-Alpine assemblage

Within the frontal Monte Rosa nappe the pre-Alpine foliation of sample 1 (Fig. 4a) is continuously dragged into a shear zone (Keller & Schmid, 2001). Thereby this pre-Alpine mineral assemblage is synkinematically replaced by an Alpine one in the case of sample 4 (Fig. 4b) (Keller *et al.*, 2004). The pre-Alpine foliation of sample 1 (Fig. 4a) is composed of biotite (0), plagioclase (0), quartz (0), kyanite (0), garnet (0), phengite (0); accessory phases include ilmenite (0), rutile (0) and tourmaline (0), the symbol '(0)' denoting pre-Alpine minerals. *P–T* conditions for the formation of the pre-Alpine assemblage were estimated at about 720°C and 8·5 kbar (Keller *et al.*, 2004). Chlorite sporadically overgrows the pre-Alpine foliation and is interpreted as an alteration product of pre-Alpine biotite (0), formed during late stages of Alpine

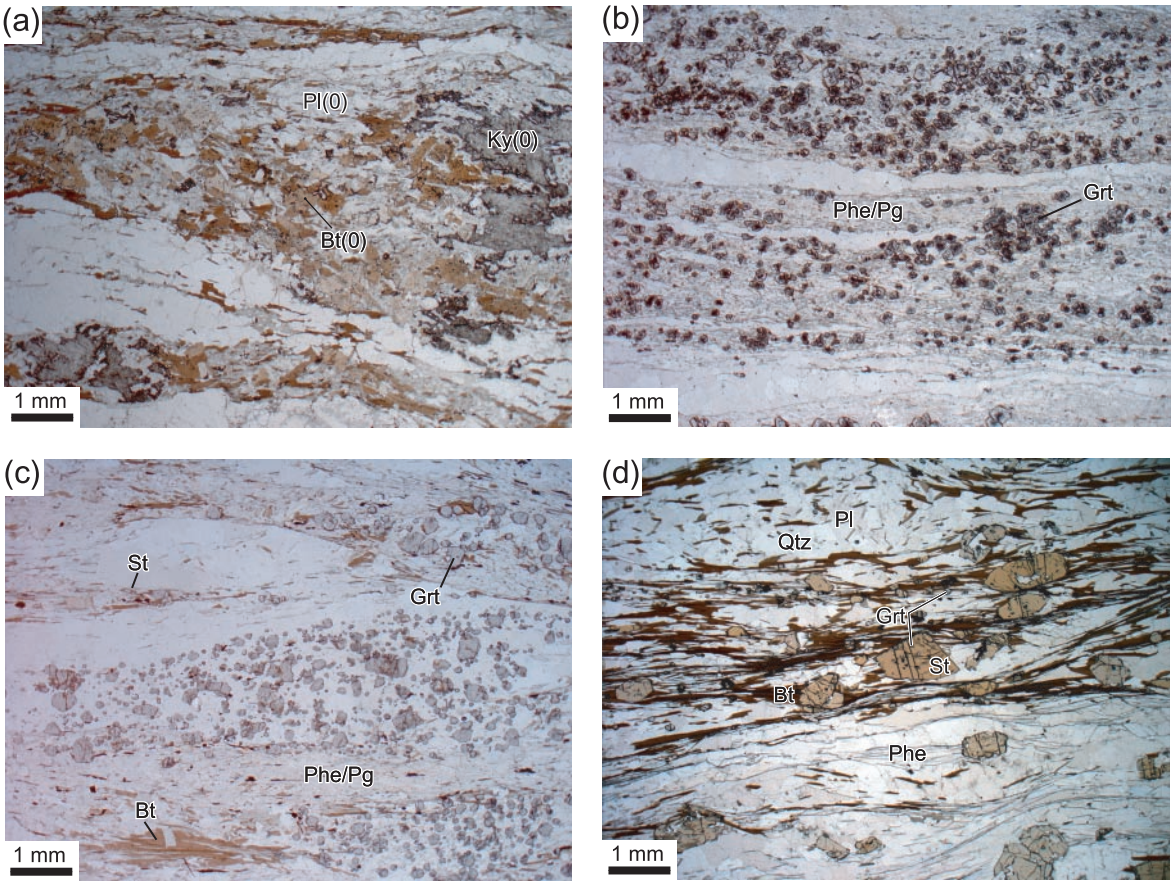

Fig. 4. Photomicrographs of thin sections providing an overview of progressive stages of the Alpine metamorphism. (a) and (b) show samples 1 and 4, respectively: the pre-Alpine assemblage Pl (0) + Bt (0) + Ky (0) (in sample 1) is replaced by an Alpine assemblage Grt + Phe + Pg of sample 4 within a shear zone and during early Alpine HP overprint [D_1–D_2 mylonitization of Keller & Schmid (2001)]. (c) and (d) show samples LK48 and LK76: continuing metamorphism during decompression and D_3 deformation (Keller *et al.*, 2005*b*), as represented by sample LK48 containing small staurolite grains and biotite in addition to the Grt + Phe + Pg. Sample LK76 also contains plagioclase but is devoid of paragonite.

metamorphism. Alpine metamorphism is indicated by a new garnet and phengite generation, both of which grow preferentially along the grain contacts between pre-Alpine biotite (0) and plagioclase (0) (Fig. 5a).

Sample 4 exhibits an early Alpine foliation, mainly composed of garnet, phengite and paragonite (Fig. 4b). According to Keller *et al.* (2004), the following reaction led to the decomposition of the pre-Alpine assemblage:

$$\mathrm{Pl(0) + Bt(0) \pm Ky(0) \pm Ilm(0) + H_2O} = \mathrm{Grt + Phe + Pg \pm Rtl.}$$

Pre-Alpine plagioclase (0) and kyanite (0) can still be detected, but their modal amount is drastically reduced compared with sample 1 (Fig. 4a and b).

Equilibrium phase diagrams predict the transformation to the first-stage assemblage Grt + Phe + Pg + Qtz in sample 4 at around 650°C and 12·5 kbar (Keller *et al.*, 2004). Conservation of the pre-Alpine assemblage in sample 1 is probably due to the absence of an aqueous fluid within the undeformed country rock of the shear zone (Keller *et al.*, 2004).

During the transformation to the Alpine assemblage the phengites became enriched in the Mg-Cel content (0·2–0·35), whereas the Fe-Cel content remained rather constant (Fig. 6, Table 2). In addition, the Pg content in phengite became slightly enriched during the Alpine transformation (Fig. 6, Table 2, see below). This indicates that the Na of the pre-Alpine plagioclase is partly stored within phengite. For a more detailed description of this early stage of Alpine metamorphism, the reader is referred to Keller *et al.* (2004).

Mineral assemblage sequence of samples 4, LK48 and LK76 (medium-Al compositions)

Starting with the first-stage assemblage Grt + Phe + Pg + Qtz of sample 4, whose formation was outlined above, biotite grows along the grain boundary of garnet and it

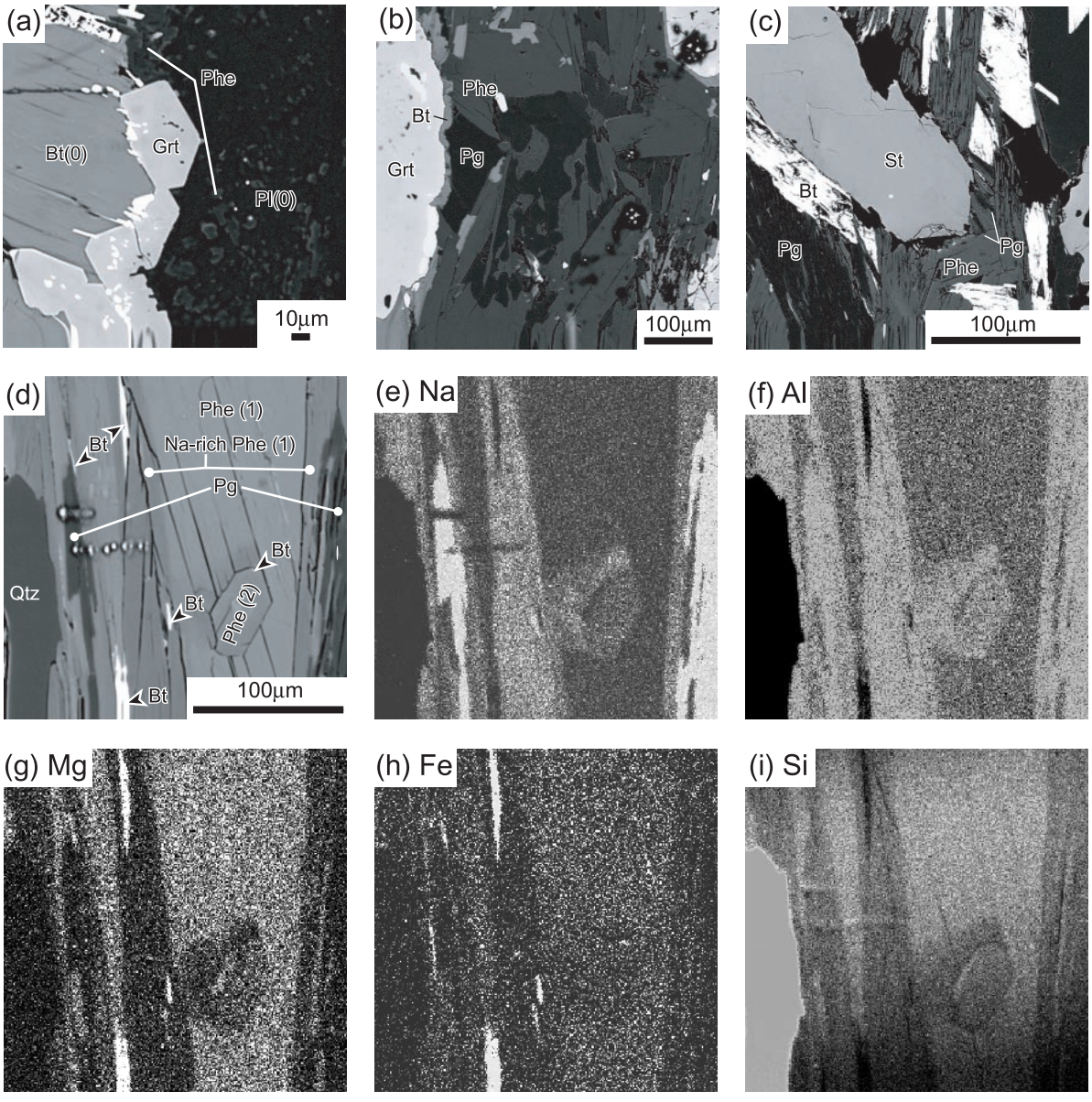

Fig. 5. Backscattered electron images (a–d) showing microstructures in samples 1, 4 and LK48. (a) Sample 1: initial stage of Alpine garnet and phengite growth along grain boundary between pre-Alpine biotite (0) and plagioclase (0). (b) Sample 4: biotite growing along the grain boundary of Alpine garnet and overgrowing paragonite and phengite. (c) Sample LK48: biotite and staurolite overgrowing phengite and paragonite. (d) Sample LK48: two phengite generations and paragonite (see below). (e–i) X-ray maps of the area shown in (d), illustrating the compositional variation of different white mica generations in sample LK48. [(e) Na; (f), Al; (g) Mg; (h) Fe; (i) Si.] Light colours correspond to a high content of a given element. The contrast was adjusted to highlight the chemical variation. The composition of the first phengite generation [Phe (1)] varies parallel to the layers: (1) layers rich in Mg, Fe and Si (high celadonite content) and poor in Na and Al; (2) layers poor in Mg, Fe and Si and rich in Na and Al. A second phengite generation [Phe (2)] overgrows the first one and is poor in Mg, Fe and Si and rich in Na and Al. (Note that biotite grows as exsolutions in layers of the first phengite generation.)

overgrows phengite and paragonite (Fig. 5b). Hence, the formation of biotite post-dates the early Alpine assemblage Grt + Phe + Pg + Qtz {1}. Accordingly biotite belongs to the second-stage assemblage Grt + Phe + Pg + Bt + Qtz {2} of sample 4.

Alteration of the early Alpine assemblage Grt + Phe + Pg + Qtz is also seen in sample LK48, which is from the CM unit and from within the staurolite zone (Fig. 2). LK48 contains garnet, phengite, paragonite, biotite, staurolite, chlorite and tourmaline as major minerals, and accessory opaque minerals. Lens-shaped garnet-rich layers and micaceous layers define the foliation (Fig. 4c).

In sample LK48 two generations of phengite are observed. A first generation [Phe (1) in Fig. 5d] is

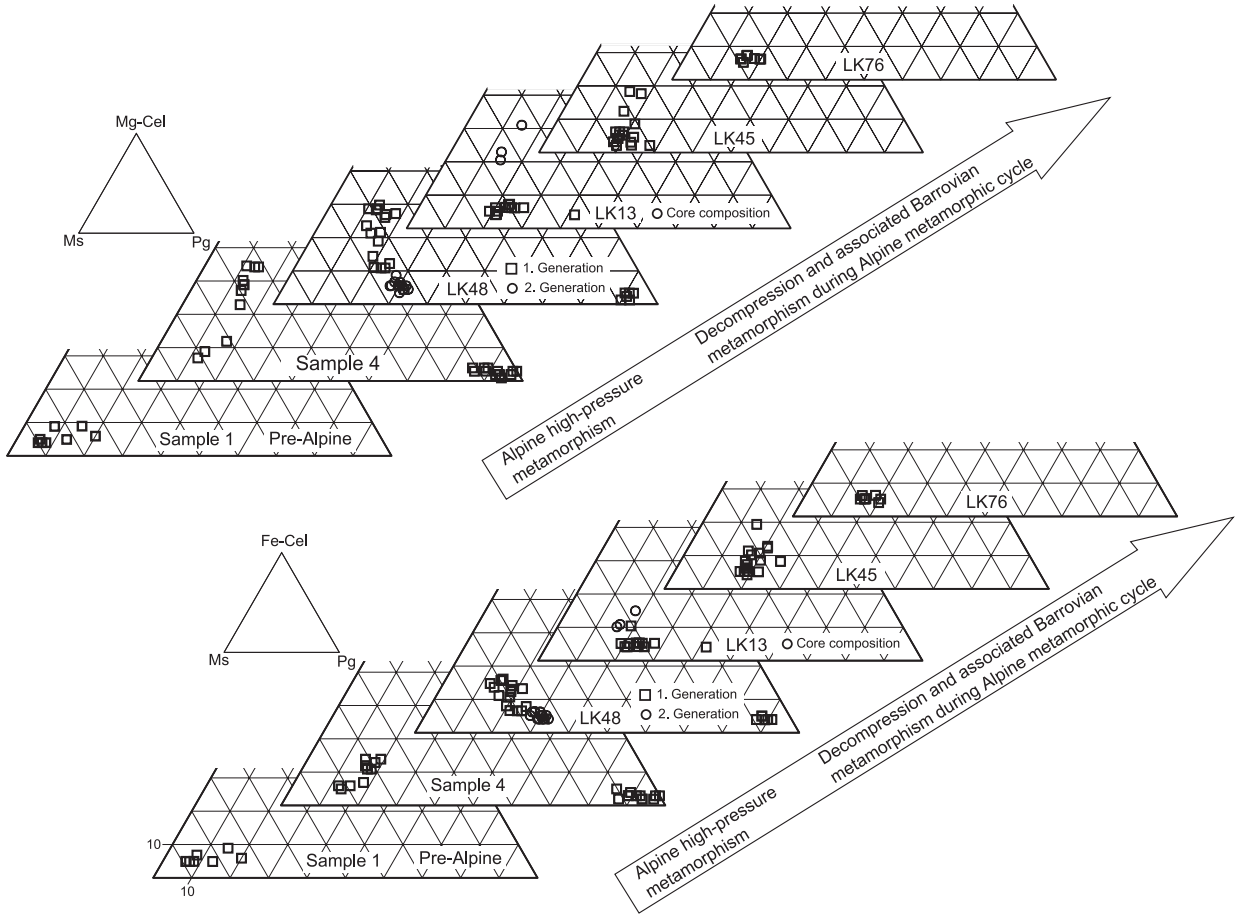

Fig. 6. White mica compositions for the studied samples in terms of paragonite (Pg), muscovite (Ms) and Mg-celadonite (Mg-Cel) or Fe-celadonite (Fe-Cel) triangular plots. There is a pronounced increase of the Mg-celadonite component related to the early high-pressure metamorphism stage whereas the Fe-celadonite component remains relatively constant. During subsequent decompression and Barrovian overprint the phengite composition changes systematically.

associated with paragonite, whereas a second phengite generation overgrows both phengite (1) and paragonite. It should be noted that the highest Na content in phengite is observed in case of the absence of plagioclase in the assemblage of sample LK48 (Fig. 6). Biotite grows as exsolution lamellae in phengite, it also overgrows paragonite, and finally it grows at the rim of garnets and staurolite (Figs 4c and 5c, d; see below). Staurolite is essentially unzoned with Mg/(Mg + Fe) of about 0·16 and it overgrows phengite (1) and paragonite, both defining the foliation (Fig. 5c). No plagioclase is detected in sample LK48. Chlorite overgrows the foliation and postdates staurolite. The microstructural relationships in sample LK48 indicate that a first stage during Alpine metamorphism is represented by the assemblage Grt + Phe (1) + Pg + Qtz {1}. The exsolution of biotite within Na-enriched phengites indicates the breakdown of phengite (1) and paragonite (Fig. 5d; see below). This leads to a second metamorphic stage represented by the assemblage Grt + Phe (2) + Pg + Bt + Qtz {2}. Evidently staurolite is produced during the breakdown of paragonite and phengite. This leads to a third metamorphic stage represented by the assemblage Grt + Phe (2) + Bt + St + Qtz {3}.

The garnets of sample LK48 are usually zoned. Where the zoning can be separated into two homogeneous parts there is a core with slightly elevated grossular and relatively low almandine contents, and a rim enriched in almandine and slightly reduced in grossular content. The pyrope content remains constant. The decrease of the grossular content corresponds to an increase in the almandine content. This same zoning pattern is also observed in garnets within pelitic rocks from the Monte Rosa nappe. There, this pattern is interpreted as the result of a two-stage growth of garnet during the first stages of Alpine metamorphism (Keller *et al.*, 2004). High grossular in the garnet cores reflects the first growth stage, during which garnet locally forms at the rims of pre-Alpine plagioclase (Fig. 5a). Low grossular in the garnet rims reflects a second growth stage, during which

Table 2: Selected microprobe analyses of white mica (for end-member calculations see text)

	Sample 1	Sample 4		LK48			LK13			LK45	LK76
	Phe	Pg	Phe	Phe 1	Pg	Phe 2	Phe (core)	Pg incl. in Pl	Phe	Phe	Phe
SiO_2	45·03	46·11	48·31	50·31	46·77	47·53	49·02	50·03	46·24	43·79	47·16
Al_2O_3	35·14	36·57	28·57	29·29	37·20	37·16	30·30	39·31	35·58	34·24	35·93
FeO	0·81	0·23	1·42	1·56	0·67	0·71	1·50	0·18	0·99	1·15	0·86
MnO	0·01	0·00	0·04	0·01	0·02	0·06	0·00	0·00	0·00	0·08	0·00
MgO	0·41	0·12	2·38	2·11	0·10	0·42	2·15	0·11	0·51	0·45	0·62
CaO	0·02	0·09	0·00	0·01	0·31	0·01	0·00	1·14	0·05	0·00	0·00
Na_2O	0·72	7·16	0·84	1·20	6·61	2·40	0·92	7·07	1·59	1·57	1·49
K_2O	10·73	0·90	9·77	9·77	1·33	8·45	10·14	0·83	9·83	8·81	9·62
TiO_2	0·80	0·03	0·73	0·50	0·26	0·53	0·64	0·27	0·88	0·36	0·55
Sum	93·67	91·21	92·06	94·76	93·27	97·27	94·67	98·94	95·67	90·45	96·23
Si	3·05	3·08	3·32	3·35	3·06	3·07	3·28	3·08	3·06	3·06	3·09
Al	0·95	0·92	0·68	0·65	0·94	0·93	0·72	0·92	0·94	0·94	0·91
Sum	4·00	4·00	4·00	4·00	4·00	4·00	4·00	4·00	4·00	4·00	4·00
Al	1·86	1·95	1·63	1·65	1·93	1·89	1·67	1·93	1·84	1·88	1·86
Fe	0·05	0·01	0·08	0·09	0·04	0·04	0·08	0·01	0·05	0·07	0·05
Ti	0·04	0·00	0·04	0·03	0·01	0·03	0·03	0·01	0·04	0·02	0·03
Mn	0·00	0·00	0·00	0·00	0·00	0·00	0·00	0·00	0·00	0·00	0·00
Mg	0·04	0·01	0·24	0·21	0·01	0·04	0·21	0·01	0·05	0·05	0·06
Sum	1·99	1·98	2·00	1·98	1·99	2·00	2·00	1·96	1·99	2·01	2·00
Na	0·09	0·93	0·11	0·16	0·84	0·30	0·12	0·84	0·20	0·21	0·19
K	0·93	0·08	0·86	0·83	0·11	0·70	0·87	0·07	0·83	0·78	0·80
Ca	0·00	0·01	0·00	0·00	0·02	0·00	0·00	0·08	0·00	0·00	0·00
Sum	1·02	1·00	0·97	0·99	0·95	1·00	0·98	0·91	1·03	1·00	0·99
X_{Ms}	0·83	0·01	0·54	0·49	0·07	0·61	0·58	0·05	0·72	0·70	0·70
X_{Pg}	0·08	0·93	0·12	0·16	0·86	0·30	0·12	0·88	0·18	0·21	0·19
$X_{Mg\text{-}Cel}$	0·04	0·03	0·25	0·24	0·02	0·04	0·21	0·03	0·05	0·03	0·06
$X_{Fe\text{-}Cel}$	0·05	0·03	0·09	0·10	0·05	0·04	0·08	0·03	0·05	0·05	0·05

garnet forms in a less Ca-rich 'effective' bulk-rock composition (Keller *et al.*, 2004).

The medium-Al sample LK76 is also taken from the CM unit, but from within the sillimanite zone (Fig. 2). It contains garnet, phengite, biotite, staurolite, sillimanite, plagioclase, rutile, chlorite and opaque minerals. Staurolite (Mg/(Mg + Fe) ~0·20) and plagioclase (An ~0·28–0·35) occur as porphyroblasts and define the foliation (Figs 4c and 7a). Rutile can be observed as inclusions in staurolite. Rare sillimanite needles (fibrolite) occur in quartz, some of them growing at the grain boundary of staurolite (Fig. 7b). Optical identification of sillimanite was confirmed by a micro-Raman analytical technique at the University of Bern. Occasionally garnet cores are resorbed, giving rise to atoll structures. Staurolite, biotite and phengite occur as inclusions in plagioclase, indicating that these two minerals pre-date plagioclase (Fig. 7a). Small garnet grains occur as inclusions in both staurolite and plagioclase indicating that these two minerals post-date garnet (Fig. 4d). The analysed phengites have a fairly homogeneous composition (Fig. 6). Chlorite is very rare and appears as the latest mineral. The microstructures indicate at least three metamorphic stages in sample LK76. Plagioclase post-dates phengite, biotite and staurolite, whereby the latter post-dates garnet. Hence, the first assemblage in sample LK76 is represented by Grt + Phe + Bt + St + Qtz {1}. The second assemblage is given by Grt + Phe + Bt + St + Pl + Qtz {2}. Sillimanite appears to post-date staurolite, which suggests that the third stage is represented by the assemblage Grt + Phe + Bt + St + Pl + Sil + Qtz {3}.

Biotite formation

Microstructures of samples 4 and LK48 indicate the formation of biotite at the expense of garnet, phengite

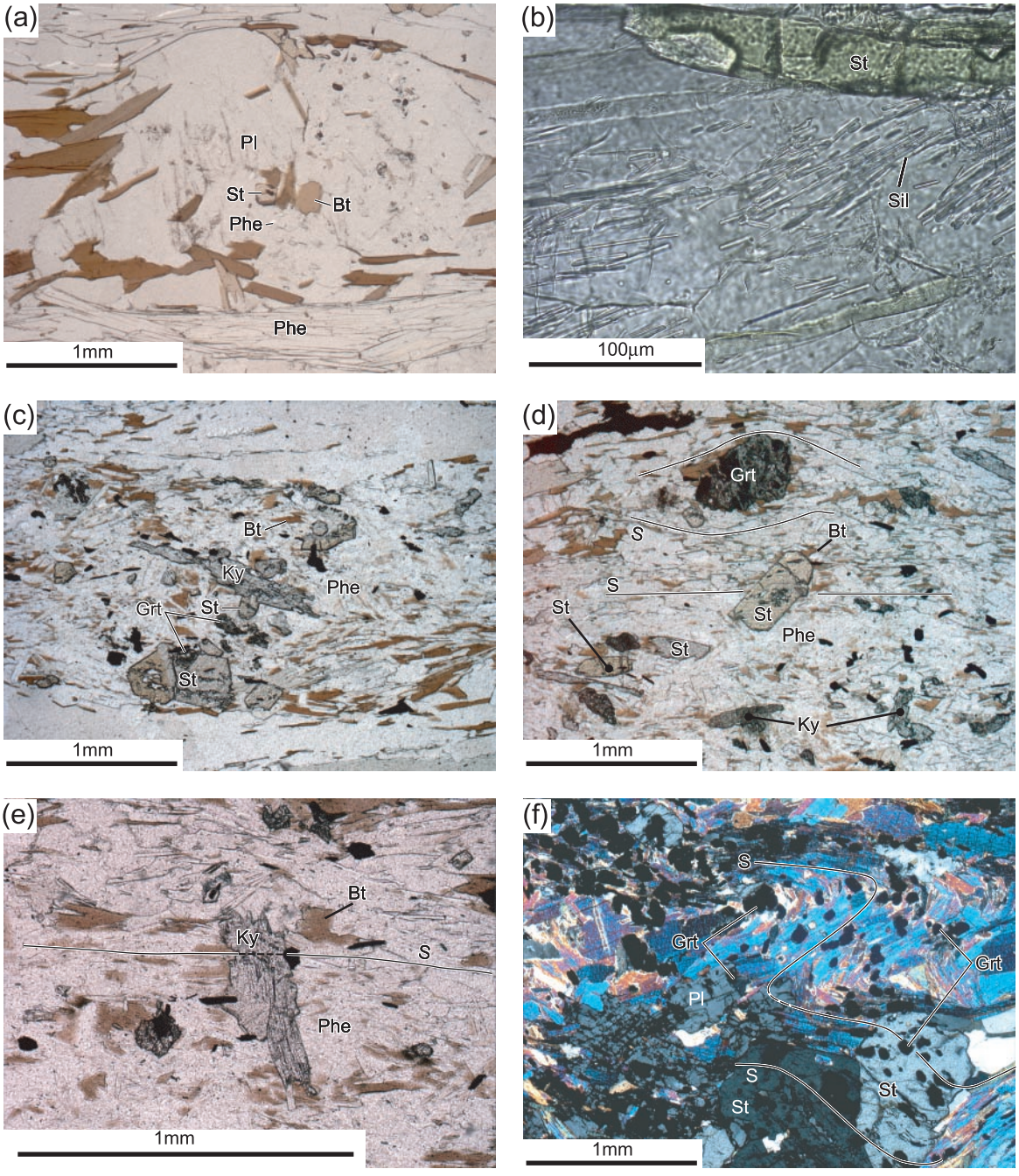

Fig. 7. Photomicrographs of thin sections to illustrate particular microstructures. (a) Sample LK76: plagioclase porphyroblast enclosing staurolite, biotite and phengite. (b) Sample LK76: sillimanite (fibrolite) growing at the rim of staurolite. (c) Sample LK13: staurolite post-dating kyanite, as it grows at the rim of kyanite. Garnet is strongly corroded. (d) Sample LK13: an early foliation (S) [S_1–S_2 of Keller *et al.* (2005*b*)] is overgrown by staurolite but curves around garnet. This indicates that staurolite post-dates garnet and grew during a later metamorphic stage. (e) Sample LK13: kyanite, also overgrowing an early formed foliation (S) [S_1–S_2 of Keller *et al.* (2005*b*)]. (f) Sample LK45: staurolite and plagioclase overgrowing a foliation (S) [S_1–S_2 of Keller *et al.* (2005*b*)], which is defined by garnet trails and mica.

and paragonite as outlined above (Fig. 5b and c). This leads to the second metamorphic stage assemblage Grt + Phe + Pg + Bt + Qtz observed in these samples. Biotite [Fe/(Fe + Mg) ~0·5], occurring in the form of exsolution lamellae, is preferentially located within domains of phengite (1), with a low Mg, Fe and Si, and a high Na and Al content (Fig. 5). This observation indicates that the Ms and the Cel contents in phengite decrease during

biotite formation. This is due to the fact that K, Mg and Fe serve as nutrients for biotite formation. Furthermore, this observation indicates that the Na content of phengite increases during the growth of biotite, indicating that Na liberated during the breakdown of paragonite is stored within phengite (Fig. 5e).

Mineral assemblage sequence of sample LK13 (low-Al composition)

Sample LK13 from the staurolite mineral zone of the CM unit (Fig. 2) contains garnet, phengite, biotite, kyanite, staurolite, plagioclase, chlorite and epidote as major minerals, and minor opaque minerals. The analysed garnets are unzoned. Paragonite occurs as inclusions in garnet and plagioclase. The foliation of the sample contains plagioclase (An ~0·27–0·31), phengite and bioite. The foliation curves around garnet porphyroblasts whereas kyanite and staurolite overgrow the foliation (Fig. 7d and e). Hence, kyanite and staurolite grew during a later stage and post-date the formation of garnet. As staurolite also grows at the rim of garnet, it is inferred that garnet decomposed during staurolite formation. Staurolite is interpreted to post-date kyanite as it grows at the rim of kyanite (Fig. 7c). Biotite [Fe/(Fe + Mg) ~0·43–0·49] defines the foliation, grows as exsolution lamellae in phengite and grows along the grain boundaries of garnet, kyanite and staurolite (Fig. 7c, d and e). These observations lead to interpretation that biotite probably belonged to the first-stage assemblage in LK13, but was also formed during the subsequent stages. Chlorite and epidote occur as the latest minerals. Phengite grains may be zoned, and Si in the cores ranges from 3·3 to 3·4 p.f.u., whereas X_{MgCel} ranges from 0·21 to 0·30 (Fig. 6, Table 2). Numerous small phengite grains show Cel contents of around 0·1 (Fig. 6, Table 2).

From these observations the following metamorphic stages and corresponding assemblages are established: Grt + Phe + Bt + Pg + Pl + Qtz {1}; Grt + Phe + Bt + Pl + Qtz {2}; Grt + Phe + Bt + Pl + Ky + Qtz {3}; Grt + Phe + Bt + Pl + Ky + St + Qtz {4}.

Mineral assemblage sequence of sample LK45 (high-Al composition)

This sample from the staurolite mineral zone in the CM unit (Fig. 2) contains garnet, phengite, biotite, staurolite, plagioclase, chlorite and opaque phases as major minerals. Abundant staurolite overgrows the matrix foliation, as is indicated by an internal foliation found in staurolite porphyroblasts (Fig. 7f). This internal foliation is slightly sigmoidal and can be traced into the matrix foliation, indicating continuing deformation during staurolite growth (Fig. 7f). Inclusion trails of garnet and opaque minerals define this internal foliation in staurolite (Fig. 7f). Phengite and biotite are also found as inclusions in staurolite. The analysed garnets show no zonation, neither in the matrix nor as inclusions in staurolite. Staurolite is unzoned with Mg/(Mg + Fe) ~0·20. Biotite is predominantly found in the matrix and defines the foliation. Inclusions of biotite are frequently found in plagioclase and only rarely in staurolite. Plagioclase porphyroblasts (An ~0·2–0·25) overgrow the foliation and post-date garnet, phengite (Si ~3·0–3·24 p.f.u.) and biotite (Fig. 7f). Chlorite appears as the last mineral. From these observations the following metamorphic stages and corresponding assemblages are established. As staurolite and plagioclase grew as porphyroblasts a first assemblage may be defined as Grt + Phe + Bt + Qtz {1}. A second assemblage probably is Grt + Phe + Bt + St + Pl + Qtz {2}. However, the microstructural evidence for the correct identification of the growth sequence of staurolite and plagioclase is equivocal. Hence, the mineral sequence of this sample will be discussed on the basis of an equilibrium phase diagram.

EQUILIBRIUM PHASE DIAGRAMS

To account for variable bulk-rock compositions we computed equilibrium diagrams for the low-Al composition of sample LK13, the medium-Al composition of sample LK48, and the high-Al composition of sample LK45 (Fig. 8). To interpret the wide range of observed phengite compositions in samples 4, LK48 and LK76 we also computed its end-member isopleths (Fig. 8b). Because the bulk-rock chemistries of samples LK48 and LK13 plot close to published average pelitic rock compositions (Fig. 3) we feel confident that the established equilibrium diagrams are more generally valid.

The use of a single bulk-rock chemistry excludes the possibility that some components may be partly locked within growing phases (e.g. cores of zoned minerals). In fact, garnet is often considered to change the effective bulk-rock composition during fractional crystallization or diffusional homogenization (Spear *et al.*, 1991; Spear, 1993). With respect to fractional crystallization the early formation of garnet possibly changed the effective bulk-rock composition representative of the decompression stages. A refractory potential is also indicated for phengite as it shows chemical zoning (Fig. 5). At high temperatures (>≈600°C), and at medium-pressure conditions, the calculated mineral abundance isopleths do not predict the growth of garnet and phengite during decompression (Fig. 9). Assuming that these predictions are correct, only components that were locked in garnet and phengite during the early growth stages should be subtracted from the initial bulk-rock composition, giving a modified effective bulk-rock composition for the early decompression stages. However, the refractory potential of garnet depends on the *T*–*t* history of the rock and the size of the garnet, whereby complete homogenization is

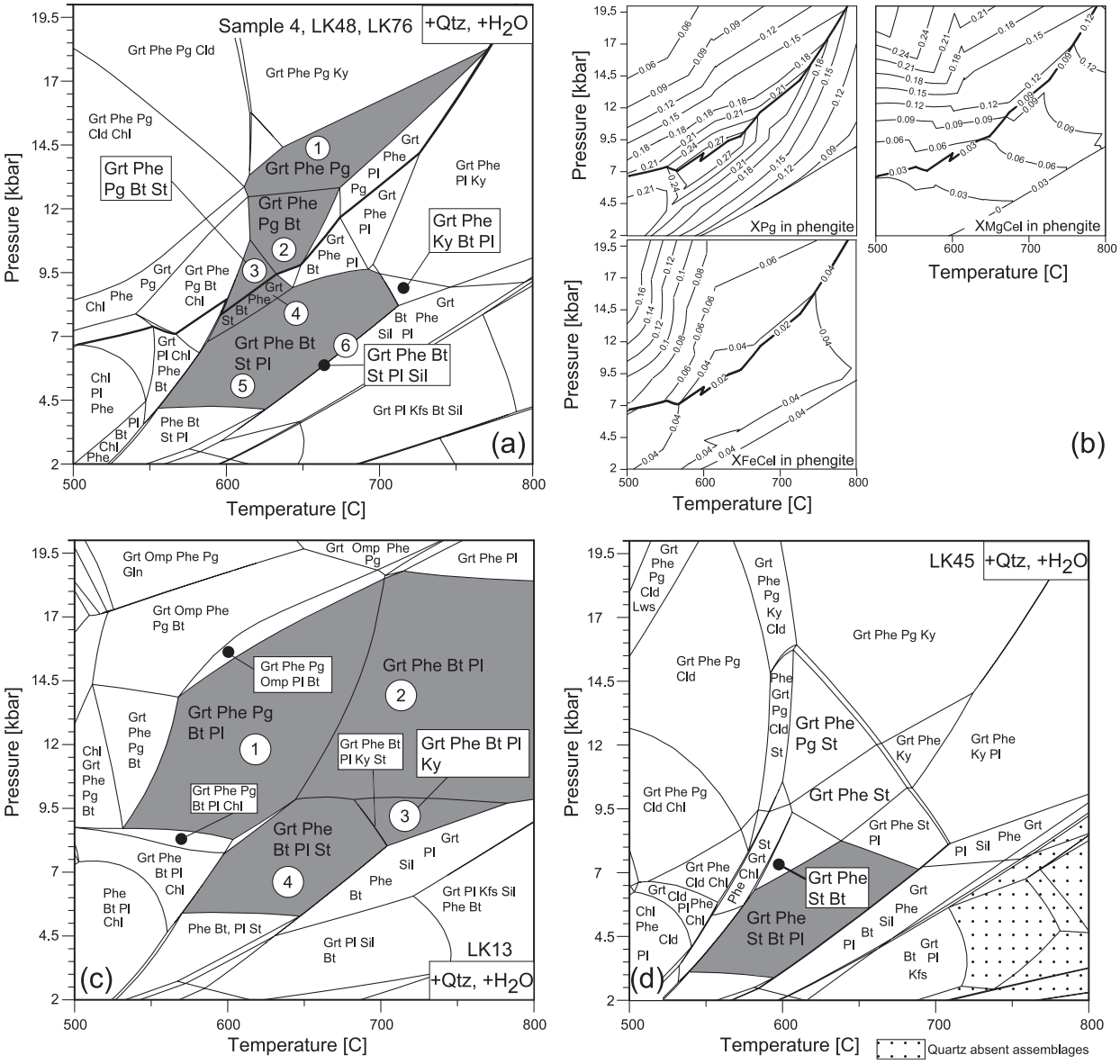

Fig. 8. Equilibrium phase diagrams for measured bulk-rock chemistries of samples LK48, LK13 and LK45, and end-member isopleths of phengite corresponding to the bulk-rock chemistry of sample LK48. The diagrams are calculated with the program DOMINO (De Capitani, 1994). They predict stable phase assemblages and corresponding mineral compositions based on thermodynamic properties defined in the database (JUN92). Bulk-rock chemistry is determined by powder X-ray diffraction and normalized to 100 cations with all iron taken as Fe^{2+}. The stability fields of successive mineral assemblages inferred from the microstructures and mentioned in the text are marked by dark shading and encircled numbers. In (a) and (b) the low-pressure stability limit of paragonite is marked by the bold line. (a) Equilibrium phase diagram for the specific bulk-rock chemistry of sample LK48, illustrating the stable mineral assemblages. (b) End-member isopleths of paragonite, Mg-celadonite and Fe-celadonite in phengite, corresponding to the bulk-rock chemistry of LK48. (c) Equilibrium phase diagram for the specific bulk-rock chemistry of sample LK13, illustrating the stable mineral assemblages. (d) Equilibrium phase diagram for the specific bulk-rock chemistry of sample LK45, illustrating the stable mineral assemblages.

predicted in garnets with radii <0·01 cm and along P–T paths with a thermal maximum of <585°C (Spear *et al.*, 1991). With the exception of very few large garnet grains, which are considered to represent relicts of the pre-Alpine assemblage, the diameter of the garnet grains in the studied samples does not exceed ≈0·5 mm (Fig. 4). In addition, relatively high temperatures (>≈600°C) are estimated, at least for the later metamorphic stages in the study area. Hence, the small garnet size and the high temperatures suggest a low refractory potential for garnet.

To test the effect of locked components on our calculations we subtracted 50% of the amount of either garnet or

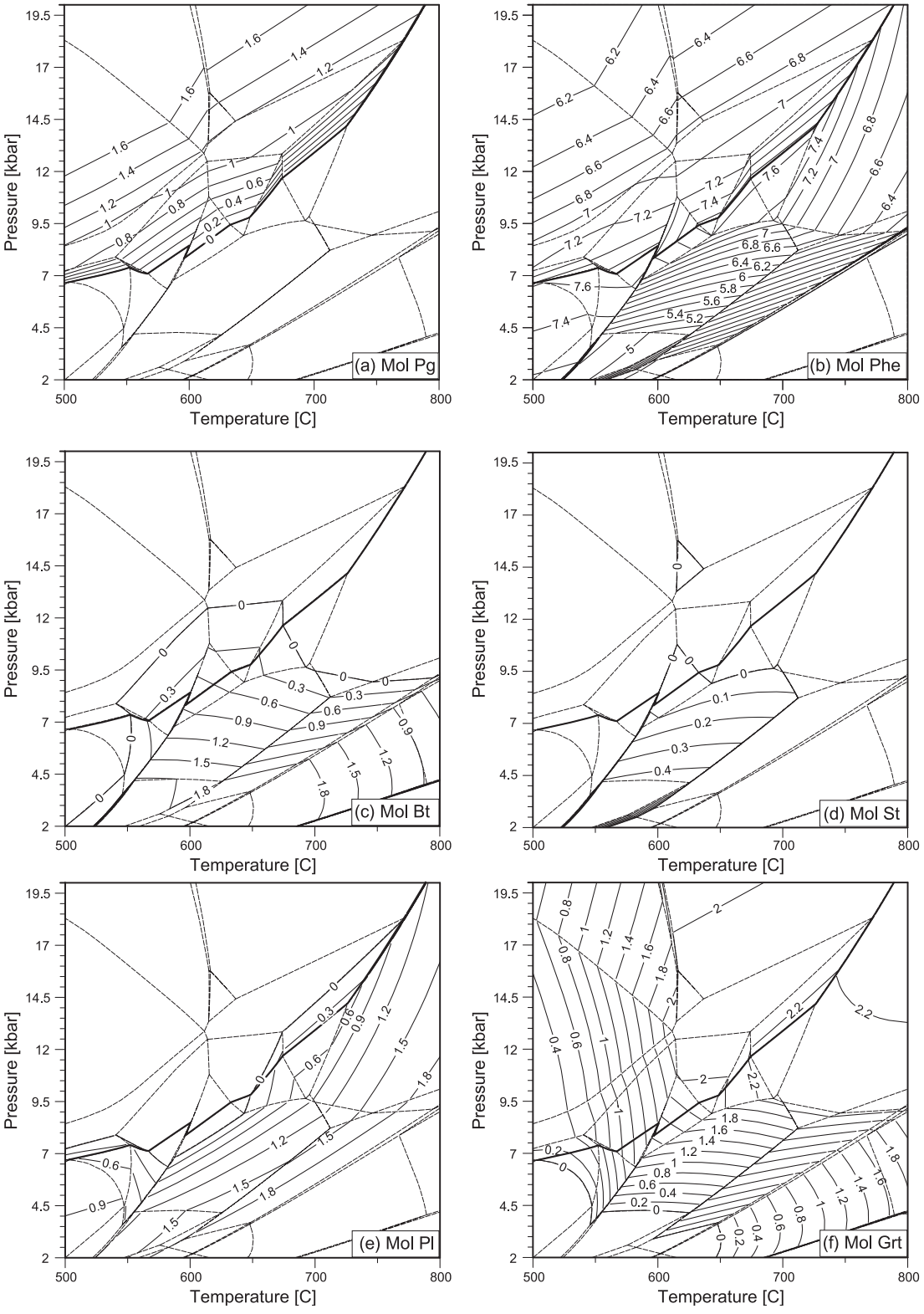

Fig. 9. Mineral abundance isopleths of paragonite (a), phengite (b), biotite (c), staurolite (d), plagioclase (e) and garnet (f). The diagrams are calculated for the measured bulk-rock chemistry of sample LK48 with the program DOMINO (De Capitani, 1994). They predict isopleths of moles of a stable phase based on thermodynamic properties defined in the database (JUN92). Bulk-rock chemistry is determined by powder X-ray diffraction and normalized to 100 cations; all iron is taken as Fe^{2+}. The low-pressure stability limit of paragonite is marked by the bold line.

white mica stable at 13 kbar and 650°C from the measured bulk-rock compositions. This test yields only minor changes in the location of the stability field boundaries calculated on the basis of these modified bulk-rock compositions in comparison with the measured ones. Based on this test, and from the fact that garnet grains are small, we feel confident that early fractional crystallization of garnet and phengite had only a minor effect on the calculated phase relations along the decompression part of the *P–T* path. It should be noted that the use of a single bulk-rock composition also ignores the potential removal or introduction of mobile components via a metamorphic fluid during decompression. All equilibrium diagrams are calculated for the system K_2O–Na_2O–CaO–FeO–MgO–Al_2O_3–SiO_2–H_2O, assuming a water activity of one.

Stable assemblages of samples LK48, 4 and LK76 (medium-Al compositions)

Figure 8a shows the equilibrium diagram calculated for the bulk-rock composition of sample LK48. The corresponding end-member isopleths of phengite are given in Fig. 8b. Shaded areas mark the successive stages of the observed Alpine assemblages. The first Alpine assemblage Grt + Phe + Pg + Qtz + H_2O (assemblage 1 in Fig. 8a) is stable within a large area above about 12·5 kbar and is interpreted to reflect peak pressure conditions. The upper pressure limit (≈16 kbar) is given by the stability of kyanite. Kyanite would become stable towards higher pressures, as continuing Tschermaks substitution would turn phengite towards less aluminous compositions, liberating aluminium for kyanite formation (Fig. 8a). Towards lower pressure the equilibrium diagram (Fig. 8a) correctly predicts the occurrence of biotite (assemblage 2 in Fig. 8a). In accordance with the measured phengite composition the calculated end-member isopleths for phengite predict both an increase in the paragonite and a decrease in the celadonite content of phengite, concomitant with biotite growth during decompression (Figs 6 and 8b). At *P–T* conditions of about 620°C and 9·5 kbar the first staurolite begins to form (see below). In sample LK48 the formation of staurolite represents the latest stage of metamorphism, preserved in form of the assemblage Grt + Phe + Pg + Bt + St + Qtz (≈620°C and 9·5 kbar; assemblage 3 in Fig. 8a). Assemblage 3 is limited towards lower pressure by the stability limit of paragonite, and the calculated phengite composition correctly predicts the highest Na content in phengite (Fig. 8b, bold line). This indicates that the second phengite generation, which is highest in Na, is in equilibrium with assemblage 3 in sample LK48, whereas the composition of the first phengite generation corresponds to earlier metamorphic stages and re-equilibration is incomplete. Towards lower pressures all paragonite is consumed by continuous reactions and the assemblage Grt + Phe + Bt + St + Qtz becomes stable (assemblage 4 in Fig. 8a). This assemblage is identified in sample LK76. This illustrates that the final replacement of paragonite does not necessarily produce plagioclase as long as all sodium from paragonite can be stored in phengite.

Growth of plagioclase and sillimanite is observed in sample LK76. The equilibrium phase diagram predicts the formation of plagioclase (assemblage 5 in Fig. 8a) towards lower pressures than those indicated by assemblage 4 in Fig. 8a. Comparison of the composition of the second generation of phengite in sample LK48 with the phengite composition of sample LK76 shows that the phengite in the plagioclase-bearing sample LK76 is richer in K (Fig. 6). This can be explained by the growth of plagioclase at the expense of Na-rich phengite. Thereby phengite changes towards a more K-rich composition, as Na is used for the formation of the albite component in plagioclase. This is in line with the end-member isopleths predicting that K in phengite increases as plagioclase grows during decompression (Fig. 8a and b). Hence, it is likely that sample LK76 experienced decompression through the plagioclase-bearing stability field of the assemblage Grt + Phe + Bt + St + Pl + Qtz. The latest metamorphic stage is represented by the growth of sillimanite at staurolite grain boundaries in sample LK76 (Fig. 7b). This is corroborated by the equilibrium phase diagram, which predicts the growth of sillimanite at the expense of staurolite at and below the low-pressure stability limit of the assemblage Grt + Phe + Bt + St + Pl + Qtz (assemblage 6 in Fig. 8a).

Stable assemblages in sample LK13 (low-Al composition)

Figure 8c shows the equilibrium diagram calculated for the bulk-rock composition of sample LK13. The dark shaded areas mark the observed mineral assemblages. The assemblage Grt + Phe + Pg + Pl + Bt + Qtz (assemblage 1 in Fig. 8c) occupies a large stability field, the upper pressure limit being given by the stability of plagioclase with respect to omphacite at pressures ranging between 14 and 18 kbar. Assemblage 1 (Fig. 8c) is interpreted to reflect peak metamorphic conditions recorded in sample LK13. It should be noted that plagioclase and biotite are stable at relatively higher pressures given the bulk-rock composition of sample LK13, when compared with the stability fields of these minerals at the bulk-rock composition of sample LK48 (Fig. 8a and c). As suggested by the A′FM projection (Fig. 3) the equilibrium diagrams verify that sample LK13 does not contain sufficient Al for storing all univalent and divalent cations in 'high aluminous minerals' such as garnet, phengite and paragonite. This increases the *P–T* area within which 'low aluminous minerals' such as biotite and plagioclase are stable.

The subsequent assemblages 2, 3 and 4 are correctly predicted by the equilibrium phase diagram. Assemblage 3 (Grt + Phe + Pl + Bt + Ky + Qtz) is limited towards lower *P–T* conditions by the stability of kyanite with respect to staurolite. The growth of staurolite at the grain boundary of kyanite indicates the formation of staurolite at the expense of kyanite (Fig. 7c). This indicates that the assemblage Grt + Phe + Pl + Bt + Ky + St + Qtz possibly represents a late metamorphic stage preserved in sample LK13, or, alternatively, that the replacement of kyanite by staurolite is sluggish because of kinetic reasons. In the latter case the sample underwent further retrogression through the *P–T* area defined by the assemblage Grt + Phe + Pl + Bt + St + Qtz where kyanite would be metastable. In any case, the observed mineral parageneses are in accordance with the prediction of the equilibrium phase diagram, and a retrogressive *P–T* path is indicated.

Stable assemblages in sample LK45 (high-Al composition)

Figure 8d shows the equilibrium diagram calculated for the rock composition of sample LK45. This sample contains the assemblage Grt + Phe + Bt + St + Pl + Qtz, which is correctly predicted by the equilibrium diagram (dark shaded area in Fig. 8d). In sample LK45 staurolite and plagioclase occur as porphyroblasts, whereby staurolite exhibits a sigmoidal internal foliation that can be traced into the matrix foliation (Fig. 7f). This foliation is predominantly defined by aligned garnet grains, whereas phengite and rare biotite are also found as inclusions in staurolite. In sample LK45 neither paragonite nor kyanite could be detected. From these observations, provided that rare biotite inclusions represent incorporations during a late stage of staurolite growth, assemblage Grt + Phe + St + Qtz can be interpreted to represent an early stage of metamorphism for sample LK45 (Fig. 8d). In this case the internal foliation of staurolite would document progressive deformation and associated growth of staurolite during the early stages of metamorphism and deformation rather than growth of staurolite over a pre-existing Alpine foliation. Figure 8d predicts the assemblage Grt + Phe + St + Qtz for a relatively restricted *P–T* area, the upper pressure limit being given by the stability of paragonite at pressures ranging between about 9·5 and 12 kbar. The stability of staurolite is limited towards higher *P–T* conditions where kyanite replaces staurolite (Fig. 8d). However, the assemblage inferred for the first Alpine stages in samples LK48 and LK13 points to somewhat higher pressures than those inferred from the assemblage Grt + Phe + St + Qtz in Fig. 8d. Because sample LK45 is from the same tectonic unit as the above two samples, it is possible that during an earlier metamorphic stage sample LK45 may also have contained paragonite, which would be stable towards higher pressures. Assuming that this interpretation is correct the porphyroblastic growth of plagioclase would indicate a late metamorphic stage in sample LK45.

MINERAL REACTIONS

It is clear that the considered five- to eight-phase assemblages in the above eight-component system are at least divariant or of even higher variance in terms of the phase rule. The high variance is largely due to the wide compositional variation of the phases present. In such high-variance assemblages the mineral reactions are continuous and mainly manifested by the gradational modal and compositional changes of a restricted group of phases. In addition, the distinct mineral parageneses observed, and the equilibrium phase diagrams, mutually indicate that the variance of the considered bulk-rock composition affects the *P–T* stability fields of stable assemblages, whereby the A′ value largely influences the formation of a specific assemblage. Based on these considerations we calculated mineral abundance diagrams for the bulk-rock composition of sample LK48, to establish the mineral reactions that cause the compositional change of phengite (Fig. 9). To account for variable A′ values we also calculated an isothermal *P*–A′ binary phase equilibrium diagram and corresponding abundance isopleths of selected minerals (Fig. 10). These calculations are made by varying the Al content of the bulk-rock composition of sample LK48, whereby the atomic ratios of the remaining components are kept constant and are those of sample LK48. The A′ values of the above-described and published pelitic compositions are indicated by arrows in Fig. 10. A constant temperature (620°C) is assumed.

In samples 4 and LK48, biotite is seen to be the first retrogressive reaction product. Biotite becomes stable towards lower pressures. In the stability field of the assemblage Grt + Phe + Pg + Bt + Qtz + H_2O (assemblage 2 in Fig. 8a) the mineral abundance isopleths predict both the continuous formation of biotite and phengite and the continuous consumption of garnet and paragonite (Fig. 9a–c and f).

From the mineral abundance isopleths and from the end-member isopleths of phengite, the following biotite-forming reaction may be formulated:

$$\text{Grt} + \text{Phe} + \text{Pg} = \text{Bt} + \text{Na, Al-richer Phe} + \text{Qtz}. \quad \text{(R1)}$$

As a result of this continuous reaction phengite becomes enriched in Na and Al towards lower pressure, which is in accordance with the measured phengite composition (Figs 5 and 6). As pressure further decreases the above reaction progresses and continually liberates more aluminium from the breakdown of paragonite and garnet. At *P–T* conditions of about 620°C at 9·5 kbar the

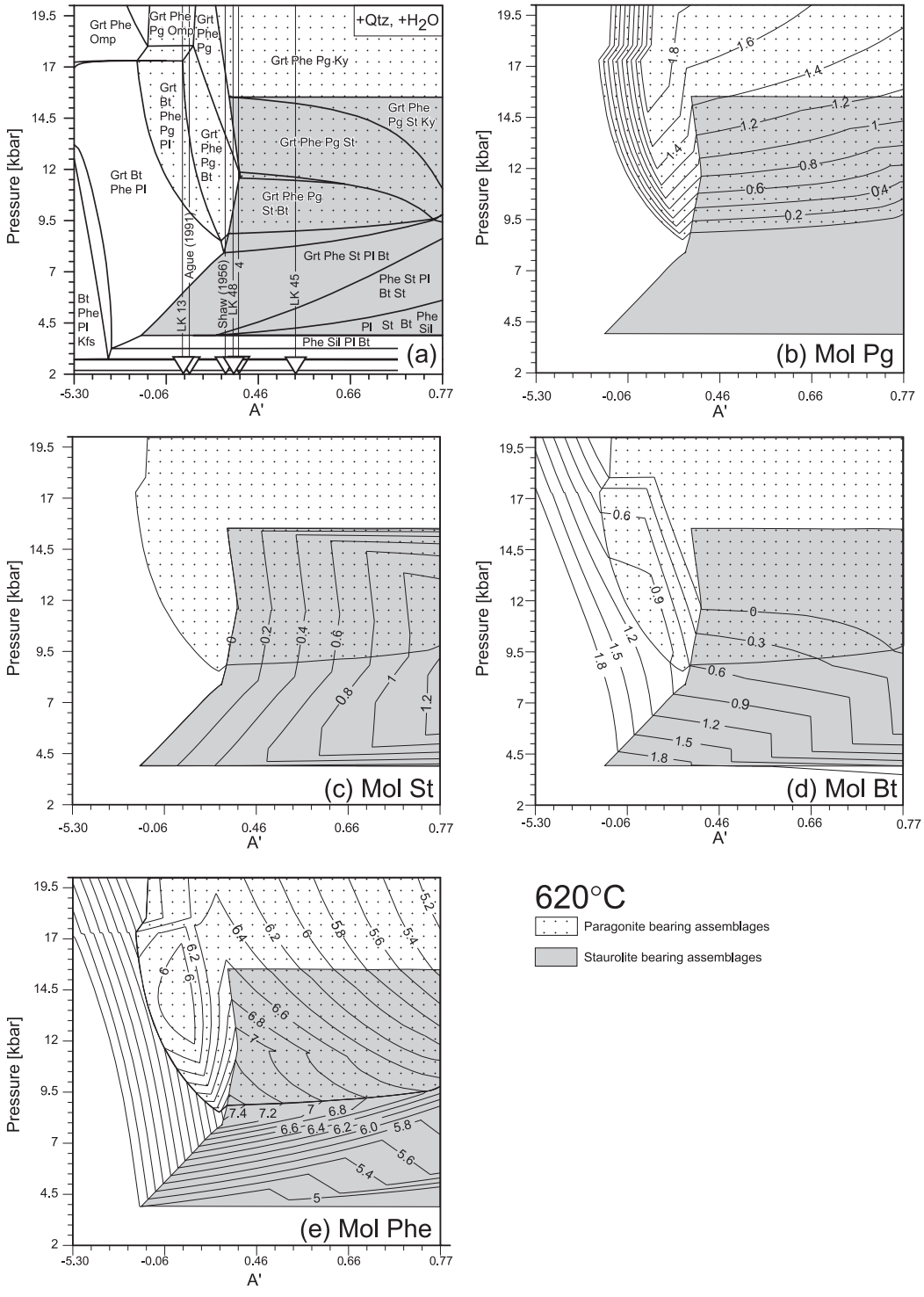

Fig. 10. *P*–A′ binary equilibrium phase diagram (a) and corresponding mineral abundance (moles) isopleths of paragonite (b), staurolite (c), biotite (d), phengite (e). Along the horizontal axis the A′ (for definition see Fig. 3) value is varied. The calculations of the diagrams are based on a variable Al content of the measured bulk-rock chemistry of sample LK48, whereas the atomic ratios of the remaining elements are held constant for different Al contents. The calculations were performed with the program DOMINO (De Capitani, 1994) and postulate distinct stable phase assemblages and isopleths of moles of a stable phase based on thermodynamic properties defined in the database (JUN92). Arrows indicate the A′ values of the described samples and of published average pelitic compositions. The grey shaded *P*–*T* areas correspond to staurolite-bearing assemblages, and the stippled *P*–*T* areas correspond to paragonite-bearing assemblages. It should be noted that the formation of staurolite is sensitive to bulk-rock composition and is related to paragonite breakdown only if the A′ values are high.

Al liberated can no longer be stored in phengite and the first staurolite is formed via the following reaction:

$$\text{Grt} + \text{Phe} + \text{Pg} = \text{St} + \text{Bt} + \text{Na, Al-richer Phe} + \text{Qtz}. \quad \text{(R2)}$$

As this reaction progresses, phengite changes towards a composition richer in Na and Al. Mineral abundance isopleths, however, indicate that only a minor amount of staurolite is formed in the course of the pressure-driven and continuous breakdown of paragonite (Fig. 9d). In addition, the *P*–A′ binary diagram and corresponding mineral abundance isopleths predict that paragonite breakdown and the concomitant formation of staurolite is restricted to higher A′ values (i.e. to Al-rich metapelites) (Fig. 10). In contrast, low-Al metapelites do not contain enough Al to store all Na in the 'high-Al' mineral phengite during decompression, and thus plagioclase is formed during the breakdown of paragonite in these rocks (Figs 8c and 10). Based on Fig. 10 the paragonite breakdown in low-Al metapelites may be formulated by the following reaction:

$$\text{Grt} + \text{Phe} + \text{Pg} = \text{Bt} + \text{Pl} + \text{Na, Al-richer Phe} + \text{Qtz} \quad \text{(R3)}$$

As a result of this continuous reaction, phengite becomes enriched in Na and Al towards lower pressure. The termination of the pressure-driven continuous reactions described so far leads to the final breakdown of paragonite, whereby its stability limit is shifted towards higher pressures for lower A′ values (i.e. for Al-poorer bulk-rock compositions) (Fig. 10). Below the stability limit of paragonite, and during continuing decompression, the continuous decomposition of Na-rich phengite and garnet forms biotite (Fig. 10). This biotite formation is independent of bulk-rock composition (Fig. 10). As biotite grows at the expense of Na-rich phengite and garnet, Na and Al are continually liberated and the mineral abundance isopleths indicate the formation of plagioclase (Fig. 9). In metapelites with higher A′ values, staurolite is formed in addition to plagioclase, and the following plagioclase- and staurolite-forming reaction may be formulated (Figs 9 and 10):

$$\text{Grt} + \text{Phe} = \text{Pl} + \text{St} + \text{Bt} + \text{K-richer Phe} + \text{Qtz} + \text{H}_2\text{O}. \quad \text{(R4)}$$

This continuous reaction forms plagioclase in metapelites with higher A′ values and takes place in the stability field of the assemblage Grt + Phe + Bt + St + Pl + Qtz found in samples LK76 and LK45 (Fig. 8a and d). In the course of the pressure-driven reaction (R4), phengite should become more K rich (Fig. 8b). In low-Al metapelites the *P*–A′ diagram and corresponding mineral abundance isopleths indicate the formation of the first staurolite via reaction (R4), which in addition proceeds to the assemblage Grt + Phe + Bt + St + Pl + Qtz, interpreted to be a late stage of sample LK13 (Figs 8c and 10). Hence, the assemblage Grt + Phe + Bt + St + Pl + Qtz, and reaction (R4), occur over a wide compositional range of pelitic compositions; mineral abundance isopleths indicate that staurolite is largely formed during the progress of reaction (R4) (i.e. during phengite breakdown) (Figs 8–10). Paragonite breakdown, however, forms only a minor amount of staurolite, and only in Al-rich bulk-rock compositions (Figs 9 and 10).

DISCUSSION

Peak metamorphic conditions

The peak metamorphic conditions for metapelites from the eastern part of the Monte Rosa nappe and the CM unit are inferred from the overlapping part of the stability fields extracted from Fig. 8a and c (fields 1 and 2 in Fig. 11). These stability fields represent the earliest Alpine metamorphic mineral assemblages found in pelitic rocks with different bulk-rock compositions. The overlapping *P*–*T* field (grey shaded in Fig. 11) allows pressure and temperature to be constrained within 12·5–16 kbar and 620–700°C, respectively. This indicates a high-pressure metamorphic stage also for the CM tectonic unit that remained undetected until now. Because the same first-stage mineral assemblage is found in medium-Al metapelites, from both the northeasternmost part of Monte Rosa nappe and the CM unit, small temperature and pressure differences are suggested for the high-pressure metamorphic stage within the study area. Therefore, we assume the same *P*–*T* conditions during high-pressure metamorphism inside the study area.

However, for the western part of the Monte Rosa nappe similar pressures (≈11–16 kbar) at somewhat lower temperatures (≈440–550°C) have been reported (Figs 1a and 11) (Chopin & Monié, 1984; Dal Piaz & Lombardo, 1986; Borghi *et al.*, 1996). Following Borghi *et al.* (1996), the Grt–Chl–Cld association commonly indicates high-pressure metamorphic conditions in metapelites of the western parts of the Monte Rosa nappe. In our calculations, this association is stable at temperatures lower than those indicated by the first-stage assemblages found in our study area (Fig. 8a and d). Hence, the high-pressure (HP) mineral assemblages in the metapelites analysed in this study, when compared with the above published data, indicate spatially different temperatures during high-pressure metamorphism (Fig. 11). This suggests that a thermal gradient prevailed during the early stages of Alpine metamorphism.

Regarding the metamorphic stages that post-date peak pressures, a metamorphic field gradient with eastwards increasing temperatures is undoubtedly indicated by the mineral zones observed in the field area (Fig. 1). Given

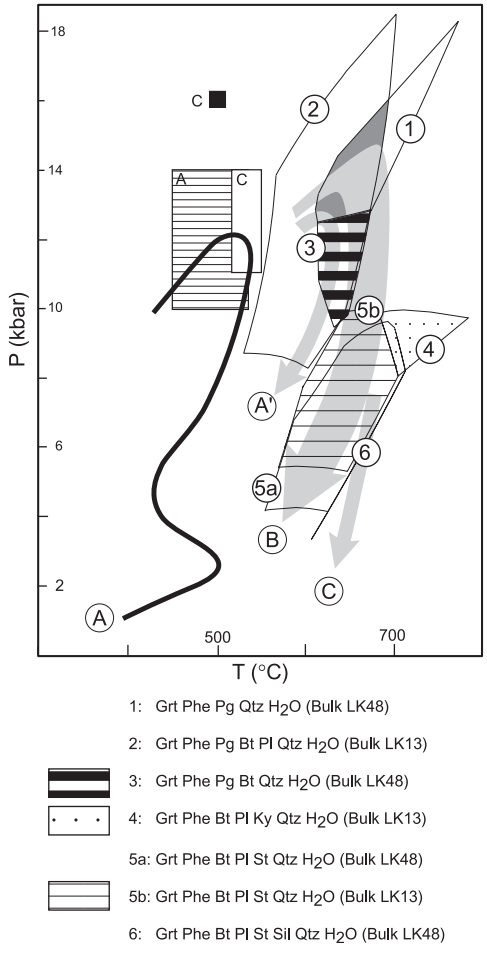

Fig. 11. Peak metamorphic conditions of the northeastern part of the Monte Rosa nappe and the CM unit as well as *P–T* paths (grey arrows and encircled A, B and C) for the studied pelitic rocks corresponding to different metamorphic zones. A, B and C indicate *P–T* conditions during the HP metamorphism for the western Monte Rosa nappe (see Fig. 1 for references and locations of *P–T* estimates). Encircled letters: A, *P–T* path for the western part of staurolite-absent mineral zone after Borghi *et al.* (1996) (location A in Fig. 1b), A′, *P–T* path for the eastern part of the staurolite-absent mineral zone (study area); B, *P–T* path for the staurolite mineral zone; C, *P–T* path for the sillimanite-bearing samples of the eastern part of the study area. Encircled numbers refer to stability fields of mineral assemblages extracted from the equilibrium diagrams of Fig. 8. The peak metamorphic conditions (grey area) are inferred from the overlapping *P–T* area of the first-stage metamorphic mineral assemblages (1) and (2) depicted in Fig. 8a and c, respectively.

the different temperatures inferred for the HP stage we propose that this metamorphic field gradient is, at least in part, inherited from the HP metamorphic stage. This is corroborated by our finding that the mineral assemblages, which are typical for Barrovian type metamorphism, undoubtedly grew at the expense of the high-pressure mineral assemblages, which are stable at higher temperatures than those reported from the western part of the Monte Rosa nappe. A more detailed discussion regarding the peak metamorphic conditions in the study area and adjacent units has been given by Keller *et al.* (2005*b*).

P–T paths

The *P–T* paths during decompression of the metapelites shown in Fig. 11 can be inferred from the mineral assemblages that are stable during the successive stages of decompression, as given by the stability fields extracted from Fig. 8a and c and explicitly shown in Fig. 11. Given this method, the precision of the *P–T* conditions defined by the *P–T* paths is limited by uncertainties regarding the calculations and the resulting variation of the position of the stability fields. Meyre *et al.* (1999), who used the same program, assumed an uncertainty of ±1 kbar and ±50°C for the absolute position of the boundaries of the stability fields. Considering the profound disequilibrium of sample LK48 and the assumed uncertainties, the relatively small stability field of Grt + Phe + Pg + Bt + St + Qtz observed in LK48 was not used to constrain the *P–T* path.

Three mineral zones can be distinguished and the corresponding *P–T* paths are labelled A, A′, B and C in Fig. 11. *P–T* path A is after Borghi *et al.* (1996) and corresponds to the western part of the Monte Rosa nappe. The different mineral zones found in the field area indicate different *P–T* conditions during the decompression part of the *P–T* paths. The *P–T* paths for metapelites from the staurolite-absent mineral zone (*P–T* paths A, A′ in Fig. 11) do not cross *P–T* areas within which staurolite is stable. This suggests that within our study area cooling is more pronounced during decompression in the case of the staurolite-absent mineral zone, where biotite, chlorite and plagioclase formed during retrogression of the metapelites (*P–T* path A′ in Fig. 11).

In contrast, the mineral parageneses of metapelites from within the staurolite mineral zone indicate nearly isothermal decompression (*P–T* path B in Fig. 11). Initial decompression during this path is constrained by the stability field of the mineral assemblage Grt + Phe + Pg + Bt + Qtz (assemblage 3 in Fig. 11) found in samples 4 and LK48, in which biotite undoubtedly grew at the expense of garnet, phengite and paragonite and by the biotite-forming reaction (R1) (Fig. 5). Towards lower pressures (~630–680°C at 9·5–10 kbar) the *P–T* path is constrained by the formation of kyanite and staurolite (assemblages 4, 5a and 5b in Fig. 11), both of which grew at the expense of assemblages stable at higher pressures (Figs 5 and 7). Similar *P–T* estimates were previously obtained for staurolite-bearing pelitic samples from the Monte Rosa nappe and from within the staurolite mineral zone (Engi *et al.*, 2001*a*). It should be noted that the clustering of stability fields along the proposed *P–T* path is within the assumed uncertainties. At low pressures massive staurolite formation occurs over large *P* interval

by the decompression-driven continuous breakdown of Na-rich phengite and garnet (Figs 9 and 10). This is indicated by the chemical change of phengite, whose paragonite content decreases from X_{Pg} ≈0·3 in the second phengite generation of sample LK48 to X_{Pg} ≈0·15–0·2 in the sillimanite-bearing sample LK76 (Figs 6 and 8a, b).

The formation of sillimanite in the eastern part of the study area (Fig. 2) may be explained by isothermal decompression at somewhat higher temperatures of about 650°C down to lower pressures of around 5 kbar (*P–T* path C in Fig. 11). In summary, the observed phase relations indicate that the eastern part of the Monte Rosa nappe and CM unit experienced amphibolite-facies conditions during near-isothermal decompression from peak *P–T* conditions. No substantial heating is necessary to explain the observed mineral parageneses.

The tectonic implications of this study [see more extensive discussion by Keller *et al.* (2005*b*)] are that Eocene-age top-to-the-north or top-to-the-NW nappe stacking (local D_1 and D_2) started under high-pressure conditions (12·5–16 kbar) and at relatively high temperatures (≈620–700°C), and also affected the CM unit, hitherto regarded as recording a Barrovian-type metamorphism only. This nappe stacking occurred during differential ascent of high-pressure units relative to surrounding units and was associated with crustal shortening. Barrovian-type metamorphism, however, initiated during a first phase of backfolding (local D_3), initiating at about 35 Ma and during the later stages of decompression. It was associated with a component of orogen-parallel extension. Unroofing by orogen-parallel extension is held responsible for delaying cooling during decompression, leading to isothermal decompression of the deeper structural levels in the eastern part of the study area. Thereby late-stage deformation (local D_3 and later) became progressively younger and prevailed at increasingly higher temperatures at the deeper structural levels exposed in the east.

End-member isopleths of phengite

The isopleths calculated for the bulk-rock composition of sample LK48, in combination with the highest Mg-celadonite content (X_{MgCel} ≈ 0·3) measured in the first phengite generation of this sample, point to pressures that are relatively higher than those obtained from metamorphic mineral assemblages stable during the first stage (Figs 6 and 8a, b). The low Mg-celadonite content of the calculated isopleths may be explained by the uncertainties of the experimental data, the lack of an activity correction for some elements (e.g. Ti, Ca, Mn) in the solution model and the assumed activity of H_2O. However, the compositional zoning and the variance of measured compositions in the first generation of phengite in sample LK48 indicates that phengite did not attain chemical equilibrium on a thin-section scale during decompression (Figs 5 and 6). Hence, the inference of quantitative *P–T* conditions from isopleths calculated for a bulk-rock composition representing a whole thin section yields equivocal results. Provided that the positions of the stability fields are only slightly affected by alteration of the bulk-rock composition during decompression (see above), the observed mineral sequence in sample LK48, combined with the equilibrium phase diagram (Fig. 8a), can be used to infer the *P–T* history within the restricted *P–T* range defined by the mineral sequence. In addition, the calculated phengite isopleths correctly predict the observed trend of phengite composition during decompression (Figs 6 and 8b).

Furthermore, the calculated isopleths for phengite predict that the Fe-celadonite content in phengite depends on temperature rather than pressure (Fig. 8d). Hence, there should only be little change in Fe-celadonite content in phengite if decompression is almost isothermal (see above). Indeed the measured Fe-celadonite contents in phengite show little variation, and they are generally lower when compared with the Mg-celadonite content (Fig. 6). Thus, the trend in the Fe-celadonite content of phengite is in accordance with the inferred *P–T* path, exhibiting almost isothermal decompression. The isopleths of Fe-celadonite should only be used qualitatively, as the determination of the Fe-celadonite content in phengite is subject to uncertainties because of the unknown amount of Fe^{3+} resulting from microprobe analysis (see also Keller *et al.*, 2005*a*).

Effects of bulk-rock composition on phengite composition during decompression

The chemical variation of phengite composition in response to changing *P–T* conditions and variable bulk-rock compositions has been discussed by Guidotti (1973), Guidotti & Sassi (1976) and Keller *et al.* (2005*a*). Hence, only a few points are discussed here. To test to what extent the Na and Cel contents in phengite are sensitive to bulk-rock composition, we calculated the end-member isopleths of paragonite and celadonite in phengite for the *P*–A′ binary diagram as indicated in Fig. 10. These isopleths, depicted in Fig. 12, reveal that the Na content in phengite depends only slightly on the A′ value (i.e. on the bulk Al content), provided that the pelitic compositions have elevated A′ values. For low A′ values the celadonite content in phengite decreases as A′ increases, whereby the Fe-celadonite content is particularly sensitive to the bulk Al content. At higher A′ values the celadonite content becomes independent of the A′ value. The A′ values of the bulk-rock compositions for samples LK48, LK76, LK45, 4 and 1 and the average pelitic composition of Shaw (1956) are high enough for the phengite composition to

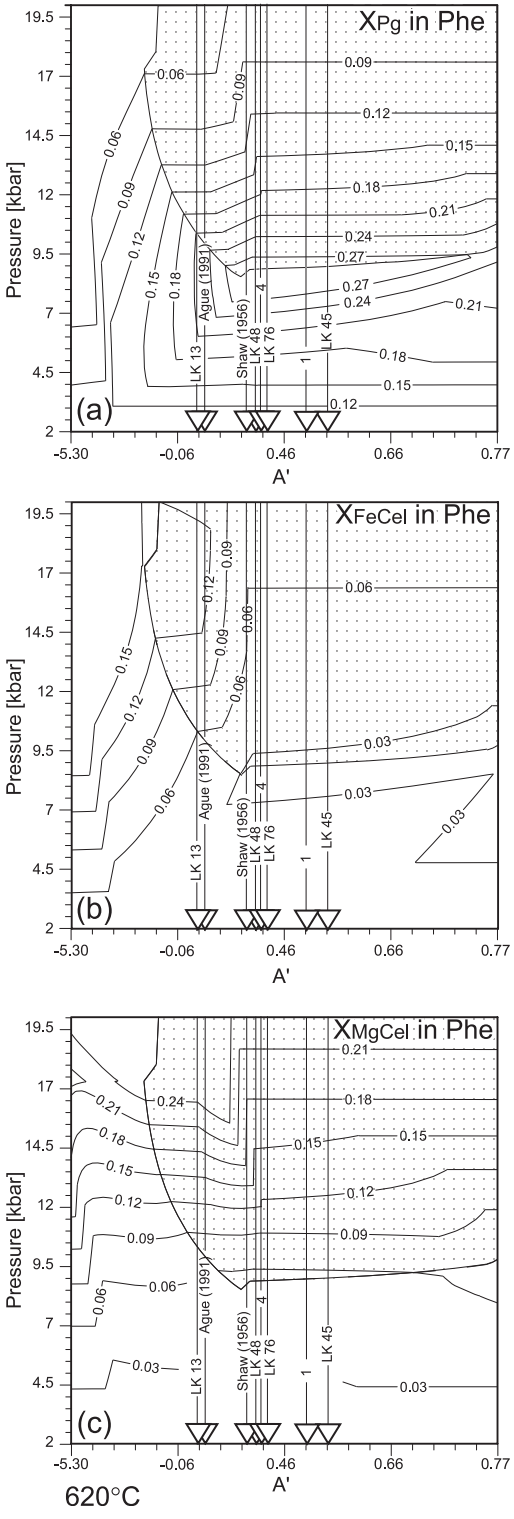

Fig. 12. End-member isopleths of paragonite (a) and celadonite (b, c) in phengite, corresponding to the *P*–A′ binary equilibrium phase diagram presented in Fig. 10. The A′ value is varied along the horizontal axis. Arrows indicate the A′ values of the described samples and of published average pelitic compositions. Dotted area indicates paragonite-bearing assemblages

be more or less independent of bulk-rock composition (Figs 10 and 12). Concerning these samples, we feel confident that the observed compositional trend of phengite solely reflects the *P–T* history of the samples, and is thus not affected by the variance of bulk-rock composition. In the case of the low-Al pelites, whose composition would, for example, correspond to that of sample LK13, or to the average pelitic composition of Ague (1991), the maximum possible Na content and the celadonite content in phengite would be sensitive to bulk-rock composition. This is in line with the results of Guidotti & Sassi (1976, 1998), showing that phengite is higher in Na and lower in Si (i.e. celadonite content) in Al-rich bulk-rock compositions than in Al-poor bulk-rock compositions.

Regional implication

In our study area the continuous breakdown of phengite largely dominates the formation of staurolite, and it occurs within a wide range of pelitic compositions (Figs 8–10). Because the formation of staurolite is related to continuous reactions within high-variance assemblages, whose stability in *P–T* space is also sensitive to bulk-rock composition, we conclude that, at least within our study area, the staurolite mineral zone boundary does not represent a simple reaction isograd indicating identical *P–T* conditions during staurolite growth all along its boundary trace in map view (Fig. 1). Slightly to the west of the staurolite mineral zone boundary paragonite is frequently found (Laduron & Martin, 1969; Laduron, 1976), whereas it can only rarely be found within this boundary. Hence, theoretically this relatively well-defined boundary could imply a reaction isograd. However, given the results of this study that indicate almost isothermal decompression, the continuous and pressure-driven reactions clearly produced this well-defined mineral zone boundary in a field area exhibiting a significant temperature gradient during staurolite formation (i.e. during decompression).

CONCLUSIONS

(1) The CM gneissic unit experienced peak high-pressure metamorphic conditions of about 620–700°C at 12·5–16·5 kbar, based on two overlapping stability fields for first-stage metamorphic mineral assemblages found within pelitic rocks of different bulk-rock compositions. Hence, temperatures during the high-pressure stage were considerably higher than those determined for the western Monte Rosa nappe.

(2) The mineral zones in the study area are characterized by Chl, Bt, Pl through St and Sil mineral zones. These indicate a metamorphic field gradient with eastwards increasing temperatures during decompression to medium pressures. The observed mineral assemblages are compatible with almost isothermal decompression. This

metamorphic field gradient is, at least in part, inherited from the high-pressure metamorphic stage. A substantial heating pulse during later stages of the metamorphic history is not necessary or indicated.

(3) The solution model for white mica, introduced by Keller *et al.* (2005*a*) and used here for calculating equilibrium diagrams, end-member isopleths of phengite and mineral abundance isopleths, gives reasonable results given that the calculations agree with the observations in natural pelitic samples. It turns out that the solution model is an important link in modelling multicomponent equilibrium diagrams for pelitic rocks as it makes the processes understandable; these are related to the decomposition of paragonite and phengite during decompression of pelitic rocks originating from high-pressure areas.

(4) At least for the gneissic units of the upper Penninic Alps, situated SW of the Simplon line, this study shows that staurolite grows within a large P interval during the continuous decomposition of paragonite and phengite, and that it is sensitive to bulk-rock composition. The observed systematic chemical variation of phengite documents the P–T history of the study area.

ACKNOWLEDGEMENTS

This work benefited from comments from and discussions with A. Berger, who also performed the micro-Raman analyses. Thorough and constructive reviews by P. O'Brien and D. Nakamura helped to substantially improve the manuscript. W. Stern and H. Hürlimann from the Geochemical Laboratory at Basel University performed the whole-rock chemical analyses. K. Waite helped with the microprobe analyses. Furthermore, we acknowledge the contributions of R. Bousquet, which were instrumental for our own thinking. This study was supported by the Swiss National Foundation Grant 20-61814.00.

REFERENCES

Ague, J. J. (1991). Evidence for major mass transfer and volume strain during regional metamorphism of pelites. *Geology* **19**, 855–858.

Barrow, G. (1912). On the geology of lower Dee-side and the southern highland border. *Proceedings of the Geologists' Association* **23**, 274–290.

Bearth, P. (1956). Zur Geologie der Wurzelzone östlich des Ossolatales. *Eclogae Geologicae Helvetiae* **49**, 267–278.

Bearth, P. (1957). Die Umbiegung von Vanzone (Valle Anzasca). *Eclogae Geologicae Helvetiae* **50**, 161–170.

Bearth, P. (1958). Ueber den Wechsel der Mineralfazies in der Wurzelzone des Penninikums. *Mineralogische und Petrographische Mitteilungen* **38**, 363–373.

Becker, H. (1993). Garnet peridotite and eclogite Sm–Nd mineral ages from the Lepontine dome (Swiss Alps): new evidence for Eocene high-pressure metamorphism in the central Alps. *Geology* **21**, 599–602.

Berman, R. G. (1988). Internally-consistent thermodynamic data for minerals in the system Na_2O–K_2O–CaO–FeO–Fe_2O–Al_2O_3–SiO_2–H_2O–CO_2. *Journal of Petrology* **29**, 445–552.

Berman, R. G. (1990). Mixing properties of Ca–Mg–Fe–Mn garnets. *American Mineralogist* **75**, 328–344.

Borghi, A., Compagnoni, R. & Sandrone, R. (1996). Composite P–T paths in the internal Penninic massifs of the western Alps: petrological constraints to their thermo-mechanical evolution. *Eclogae Geologicae Helvetiae* **89**, 345–367.

Bowtell, S. A., Cliff, R. A. & Barnicoat, A. C. (1994). Sm–Nd isotopic evidence on the age of eclogitization in the Zermatt–Saas ophiolite. *Journal of Metamorphic Geology* **12**, 187–196.

Bucher, K. & Frey, M. (1994). *Petrogenesis of Metamorphic Rocks*. Berlin: Springer.

Chopin, C. & Monié, P. (1984). A unique magnesiochloritoid-bearing, high-pressure assemblage from the Monte Rosa, Western Alps: petrologic and ^{40}Ar–^{39}Ar radiometric study. *Contributions to Mineralogy and Petrology* **87**, 388–398.

Colombi, A. (1989). Métamorphisme et géochimie des roches mafiques des Alpes ouest–centrales (géoprofile Viège–Domodossola–Locarno). *Mémoires de Géologie, Lausanne* **4**, 1–216.

Colombi, A. & Pfeifer, H.-R. (1986). Ferrogabbroic and basaltic metaeclogites from the Antrona mafic–ultramafic complex and Centovalli–Locarno region (Italy and Southern Switzerland)—first results. *Schweizerische Mineralogische und Petrographische Mitteilungen* **66**, 99–110.

Dal Piaz, G. V. (1999). The Austroalpine–Piedmont nappe stack and the puzzle of the Alpine Tethys. *Memorie di Science Geologiche* **51**, 155–176.

Dal Piaz, G. V. & Lombardo, B. (1986). Early Alpine eclogite metamorphism in the Penninic Monte Rosa–Gran Paradiso basement nappes of the northwestern Alps. In: Evans, B. W. & Brown, E. H. (eds) *Blueschists and Eclogites. Geological Society of America, Memoirs* **164**, 249–265.

De Capitani, C. (1994). Gleichgewichts-Phasendiagramme: Theorie und Software. *Berichte der Deutschen Mineralogischen Gesellschaft, Beihefte zum European Journal of Mineralogy* **6**, 48.

De Capitani, C. & Brown, T. H. (1987). The computation of chemical equilibrium in complex systems containing non-ideal solutions. *Geochimica et Cosmochimica Acta* **51**, 2639–2652.

Duchene, S., Blichert-Toft, J., Luais, B., Télouk, P., Lardeaux, J. M. & Albarède, F. (1997). The Lu–Hf dating of garnets and the ages of Alpine high-pressure metamorphism. *Nature* **387**, 586–588.

Engi, M, Todd, C. S. & Schmatz, D. R. (1995). Tertiary metamorphic conditions in the eastern Lepontine Alp. *Schweizerische Mineralogische und Petrographische Mitteilungen* **75**, 347–369.

Engi, M., Scherrer, N. C. & Burri, T. (2001*a*). Metamorphic evolution of pelitic rocks of the Monte Rosa nappe: constraints from petrology and single grain monazite age data. *Schweizerische Mineralogische und Petrographische Mitteilungen* **81**, 305–328.

Engi, M., Berger, A. & Roselle, G. T. (2001*b*). Role of the tectonic accretion channel in collision orogeny. *Geology* **29**, 1143–1146.

Escher, A., Hunziker, J. C., Marthaler, M., Masson, H., Sartori, M. & Steck, A. (1997). Geologic framework and structural evolution of the western Swiss–Italian Alps. In: Pfiffner, O. A., Lehner, P., Heitzmann, P., Mueller, St. & Steck, A. (eds) *Deep Structure of the Alps, Results of NRP 20*. Basel: Birkhäuser, pp. 205–222.

Fox, J. S. (1975). Three-dimensional isograds from the Lukmanier Pass, Switzerland, and their tectonic significance. *Geological Magazine* **112**, 547–626.

Frey, M., Hunziker, J. C., Neil, J. R. & Schwander, H. W. (1976). Equilibrium–disequilibrium relations in the Monte Rosa Granite, Western Alps: petrological, Rb–Sr and stable isotope data. *Contributions to Mineralogy and Petrology* **55**, 147–179.

Frey, M., Desmons, J. & Neubauer, F. (eds) (1999). Metamorphic maps of the Alps. Published by the editors and as enclosure to *Schweizerische Mineralogische und Petrographische Mitteilungen* **79.**

Fuhrman, M. L. & Lindsley, D. H. (1988). Ternary-feldspar modelling and thermometry. *American Mineralogist* **73**, 201–215.

Gregurek, D., Abart, R. & Hoinkes, G. (1997). Contrasting Eoalpine *P–T* evolution in the southern Koralpe, Eastern Alps. *Mineralogy and Petrology* **60**, 61–80.

Guidotti, C. V. (1973). Compositional variation of muscovite as a function of metamorphic grade and assemblages in metapelites from N. W. Maine. *Contributions to Mineralogy and Petrology* **42**, 33–42.

Guidotti, C. V. & Sassi, F. P. (1976). Muscovite as a petrogenetic indicator mineral in pelitic schists. *Neues Jahrbuch für Mineralogie, Abhandlungen* **127**, 97–142.

Guidotti, C. V. & Sassi, F. P. (1998). Petrogenetic significance of Na–K white mica mineralogy: recent advances for metamorphic rocks. *European Journal of Mineralogy* **10**, 815–854.

Heinrich, C. A. (1986). Eclogite facies regional metamorphism of hydrous mafic rocks in the central Alpine Adula nappe. *Journal of Petrology* **27**, 123–154.

Hunziker, J. C. (1970). Polymetamorphism in the Monte Rosa, Western Alps. *Eclogae Geologicae Helvetiae* **63**, 151–161.

Hunziker, P. (2003). The stability of tri-octahedral Fe^{2+}–Mg–Al chlorite. A combined experimental and theoretical study. Ph.D. thesis, University of Basel, 162 pp.

Keller, L. M. & Schmid, S. M. (2001). On the kinematics of shearing near the top of the Monte Rosa nappe and the nature of the Furgg zone in the Val Loranco Antrona valley, N. Italy: tectono-metamorphic and paleogeographical consequences. *Schweizerische Mineralogische und Petrographische Mitteilungen* **81**, 347–367.

Keller, L. M., Abart, R., Stünitz, H. & De Capitani, C. (2004). Deformation, mass transfer and mineral reactions in an eclogite facies shear zone in a polymetamorphic metapelite (Monte Rosa nappe, western Alps). *Journal of Metamorphic Geology* **22**, 97–118.

Keller, L. M., De Capitani, C. & Abart, R. (2005*a*). A quaternary solution model for white micas based on natural coexisting phengite–paragonite pairs. *Journal of Petrology* **46**, doi:10.1093/petrology/egi050.

Keller, L. M., Hess, M., Fügenschuh, B. & Schmid, S. M. (2005*b*). Structural and metamorphic evolution of the Camughera–Moncucco, Antrona and Monte Rosa units southwest of the Simplon line, Western Alps. *Eclogae Geologicae Helvetiae* **98**, 21–52.

Klein, J. A. (1978). Post-nappe folding southeast of the Mischabel Rückfalte (Pennine Alps) and some aspects of the associated metamorpism. *Leidse Geologische Mededelingen* **51**, 233–312.

Laduron, D. (1976). L'antiforme de Vanzone. Etude pétrologique et structurale dans la valle Anazasca (Province de Novara, Italie). *Mémoires de l'Institut de Géologie de l'Université de Louvain* **28**, 1–121.

Laduron, D. & Martin, H. (1969). Coexistence de paragonite et muscovite et phengite dans un micaschist à grenat de la zone du Mont-Rose. *Annales de la Societé Géologique de Belgique* **92**, 159–172.

Merlyn, M. (1977). Structure et metamorphisme du complexe Camughera–Moncucco entre la Valle Anzasca et le Val Brevettola (Province de Novara, Italie). Ph.D. thesis, Université catholique de Louvain.

Meyre, C., De Capitani, C. & Partsch, J. H. (1997). A ternary solid solution model for omphacite and its application to geothermobarometry of eclogites from the middle Adula nappe (CentralAlps, Switzerland). *Journal of Metamorphic Geology* **15**, 687–700.

Meyre, C., De Capitani, C., Zack, T. & Frey, M. (1999). Petrology of high-pressure metapelites from the Adula nappe (Central Alps, Switzerland). *Journal of Petrology* **40**, 199–213.

Milnes, A. G., Greller, M. & Müller, R. (1981). Sequence and style of major post-nappe structures, Simplon–Pennine Alps. *Journal of Structural Geology* **3**, 411–420.

Nagel, T., De Capitani, C. & Frey, M. (2002). Isograds and *P–T* evolution in the Southeastern Lepontine Dome (Graubünden, Switzerland). *Journal of Metamorphic Geology* **20**, 309–324.

Niggli, E. (1970). Alpine Metamorphose und alpine Gebirgsbildung. *Fortschritte der Mineralogie* **47**, 16–26.

Oberhänsli, R., Bousquet, R., Engi, M., Goffé, B., Gosso, G., Handy, M., Höck, V., Koller, F., Lardeaux, J.-M., Poliano, R., Rossi, P., Schuster, R., Schwarz, S. & Spalla, M. (2004). *Metamorphic Structure of the Alps* (1:1 000 000). Paris: Commission for the Geological Map of the World (UNESCO).

Reinhardt, B. (1966). Geologie und Petrographie der Monte Rosa Zone, der Sesia Zone und des Canavese im Gebiet zwischen Valle d'Ossola und Valle Loana. *Schweizerische Mineralogische und Petrographische Mitteilungen* **46**, 553–678.

Rubatto, D., Gebauer, D. & Compagnoni, R. (1997). Dating the UHP/HP metamorphism in the western Alps Sesia–Lanzo and Zermatt–Saas–Fee: evidence for subduction events at the Cretaceous–Tertiary boundary in the Middle Eocene. Fifth International Eclogite Conference, Ascona. *Terra Nova* **9**(Supplement 1), 30–31.

Schmid, S. M., Fügenschuh, B., Kissling, E. & Schuster, R. (2004). Tectonic map and overall architecture of the Alpine orogen. *Eclogae Geologicae Helvetiae* **97**, 93–117.

Shaw, D. M. (1956). Geochemistry of pelitic rocks. Part 3: Major elements and general geochemistry. *Geological Society of America Bulletin* **67**, 919–934.

Spear, F. S. (1993). *Metamorphic Phase Equilibria and Pressure–Temperature–Time Paths. Mineralogical Society of America Monograph.*

Spear, F. S., Kohn, M. J., Florence, F. P. & Menard, T. (1991). A model for garnet and plagioclase growth in pelitic schists: implications for thermobarometry and *P–T* path determinations. *Journal of Metamorphic Geology* **8**, 683–696.

Spicher, A. (1976). Tektonische Karte der Schweiz 1:500 000. Schweizerische Geologische Kommission. Wabern: Bundesamt für Landestopographie.

Thompson, J. B. (1957). The graphical analysis of the mineral assemblages in pelitic schists. *American Mineralogist* **42**, 842–858.

Todd, C. S. & Engi, M. (1997). Metamorphic field gradients in the Central Alps. *Journal of Metamorphic Geology* **15**, 513–530.